NON-SYNCHRONOUS VIBRATION OF TURBOMACHINERY AIRFOILS

AFOSR Contract F49620-03-1-0204

Final Report

By

Robert E. Kielb, Senior Research Scientist and Principal Investigator
Kenneth C. Hall, Professor & Chair
Meredith Spiker, Graduate Student
Jeffrey P. Thomas, Research Assistant Professor

Department of Mechanical Engineering and Materials Science
Edmund T. Pratt, Jr. School of Engineering
Duke University
Durham, NC 27708-0300

Lt. Col. Rhett Jeffries
AFOSR Program Manager
AFOSR/NA
875 North Randolph Street
Suite 325, Room 3112
Arlington, VA 22203-1768

REPORT DOCUMENTATION PAGE

Form Approved
OMB No. 0704-0188

PLEASE DO NOT RETURN YOUR FORM TO THE ABOVE ADDRESS.

1. REPORT DATE *(DD-MM-YYYY)*	2. REPORT TYPE	3. DATES COVERED *(From - To)*
30-05-2006	Final Performance	01-04-2003 to 28-02-2006

4. TITLE AND SUBTITLE

Non-Synchronous Vibration of Turbomachinery Airfoils

5a. CONTRACT NUMBER

5b. GRANT NUMBER

F49620-03-1-0204

5c. PROGRAM ELEMENT NUMBER

6. AUTHOR(S)

Kielb, Robert, E. Senior Research Scientist and Principal Investigator
Hall, Kenneth, C, Professor & Chair
Spiker, Meredith, A, Graduate Student
Thomas, Jeffrey, P. Research Assistant Professor

5d. PROJECT NUMBER

5e. TASK NUMBER

5f. WORK UNIT NUMBER

7. PERFORMING ORGANIZATION NAME(S) AND ADDRESS(ES)

Department of Mechanical Engineering and Materials Science
Edmund T. Pratt, Jr. School of Engineering
Duke University
Durham, NC 27008-0300

8. PERFORMING ORGANIZATION REPORT NUMBER

9. SPONSORING/MONITORING AGENCY NAME(S) AND ADDRESS(ES)

Lt. Col. Rhett Jeffries
AFOSR Program Manager
875 North Randolph Street
Suite 325, Room 3112
Arlington, VA 22203-1768

10. SPONSOR/MONITOR'S ACRONYM(S)

11. SPONSOR/MONITOR'S REPORT NUMBER(S)

AFRL-SR-AR-TR-06-0269

12. DISTRIBUTION/AVAILABILITY STATEMENT

Approved for public release; distribution is unlimited

13. SUPPLEMENTARY NOTES

14. ABSTRACT

The goal of this research was to develop a fast computational method to be able to understand non-synchronous vibrations in turbomachinery blades in the design stage. The numerical approach involved the use of a two- and three-dimensional nonlinear Navier-
Stokes unsteady harmonic balance method. As an initial demonstration of the method, the flow over a cylinder and a two-dimensional
airfoil, the 2D C1 case, were investigated and results showed good agreement. For the 3D C1 case and a running tip clearance of 0.020 in.,
two irrational frequencies were present in the solution so the current HB method could not be used. In order to justify the merits of the HB
method, a tighter tip clearance of 0.002 in. was studied. The HB method showed good agreement with the time domain results for the

15. SUBJECT TERMS

turbomachinery, blade vibrations, flutter, harmonic balance

16. SECURITY CLASSIFICATION OF:			17. LIMITATION OF ABSTRACT	18. NUMBER OF PAGES	19a. NAME OF RESPONSIBLE PERSON
a. REPORT	b. ABSTRACT	c. THIS PAGE			Robert Kielb
Uncalssified	Unclassified	Unclassified		72	19b. TELEPHONE NUMBER *(Include area code)* 919-660-5327

TABLE OF CONTENTS

1. INTRODUCTION

Currently, in turbomachinery, the two main design considerations are blade forced response and flutter. Forced response of the blades result due to aerodynamic excitations from upstream wakes and occur at integer multiples of the vane passing frequency. Flutter is a self-excited aeroelastic instability in which the aerodynamic forces on the blade add to the blade vibration itself. In both these cases, the vibrations can be large enough to cause the blades to fracture. However, in recent years, engine manufacturers have encountered a new class of aeromechanical problems. This category generally includes separated flow vibrations (SFV) and non-synchronous vibrations (NSV). Separated flow vibrations are similar to buffeting in wings and occur when an unsteady, separated flow is generated over a row of turbine blades that randomly excites blade vibration (Hall 2004, 675). In addition, they generally have a broadband frequency content. Non-synchronous vibrations are similar to separated flow vibrations except they are usually well-ordered, can occur away from a stalled condition, and occur at one dominant frequency. The blade vibrations are generally frequency and phase locked. Typical non-turbulent examples of these phenomena include the vortex shedding flow over a car antenna, power lines, cables, or off-shore risers and all can cause large amplitude vibrations. Although both non-synchronous vibrations and separated flow vibrations are emerging research areas, this effort is only concerned with the study and prevention of non-synchronous vibrations.

Non-synchronous vibrations in turbine engine blades are the result of the interaction of an aerodynamic instability, such as vortex shedding, with the vibrations of the blades. It is a serious aeroelastic problem that has been observed by most engine

companies and can ultimately lead to blade fracture. Currently, there is limited knowledge of this phenomenon, so failures typically do not occur until the testing phase. As a result, engineers must redesign the blade or the rotor. This procedure is costly and greatly increases production time.

Therefore, the overall goal of the NSV research effort at Duke is to develop a fast, systematic method for engine companies to prevent and eliminate NSV. This will be accomplished by using a novel computational fluid dynamic technique, namely the nonlinear, unsteady harmonic balance method developed by Hall, et al. to solve the three-dimensional Reynolds averaged Navier-Stokes equations governing the flow through an engine blade passage (Hall, Thomas, and Clark 2002, 879). This method offers distinct computational advantages over currently used methods. In particular, it requires one to two orders of magnitude less computational time than conventional time marching computational fluid dynamic (CFD) methods (Hall, Thomas, and Clark 2002, 886). Furthermore, the harmonic balance method can handle large flow disturbances while time-linearized equations are only valid for small unsteady perturbations. However, typically in a flow analysis, the oscillation frequency is known beforehand and therefore serves as an input to the system. Since the goal of the research is to find the NSV frequency, a new phase error method is employed to achieve quick solution convergence. This novel frequency search technique utilizes the phase difference between successive iterations of an unsteady first harmonic quantity such as unsteady lift and was developed by Kenneth Hall (private communication). It requires only a few harmonic balance solution computations to determine the precise NSV frequency. This method will be described in detail in the latter portion of the theory section. Therefore, by integrating

these numerical solution techniques, a more computationally efficient method for predicting both the NSV frequency and amplitude will be developed.

An accurate prediction of the NSV is important because it provides useful Campbell diagram information for rotating blade design purposes. A hypothetical Campbell diagram is presented in Figure 1. The Campbell diagram is a plot of the blade's natural frequencies of vibration in Hz as a function of the rotational speed of the engine in RPM. The diagonal lines of constant slope represent engine order excitations lines, i.e. multiples of the operation speed or machine harmonics. The nearly horizontal lines represent natural frequencies of particular blade modes, i.e. first flex (1F) or first torsion (1T). As a result of the harmonic balance analysis, the NSV frequencies could be added to the Campbell diagram to identify regions where the frequency of the flow instability might interact with a blade natural frequency, resulting in blade vibrations. These possible points of intersection have been identified on the Campbell diagram. Presently, engineers commonly use the Campbell diagram to determine potential resonant response problems by examining the crossing synchronous excitations (such as vane passings) with the blade natural frequencies. In addition, the presence of asynchronous vibrations such as flutter can be determined by examining the Campbell diagram. For all cases, the stress levels at the crossing points can be high enough to cause high cycle fatigue of the blades and therefore, greatly reduce the component's life span. However, other aeromechanical problems such as SFV and NSV are not presently placed on a Campbell diagram because they are not well enough understood and a design analysis method has not yet been developed. Therefore, the proposed method, when extended to blades, will allow engineers to better understand NSV behavior and to predict the

occurrence of vortex-induced vibrations. Once this fluid dynamic instability becomes better understood, it will be possible to couple the NSV with blade motion.

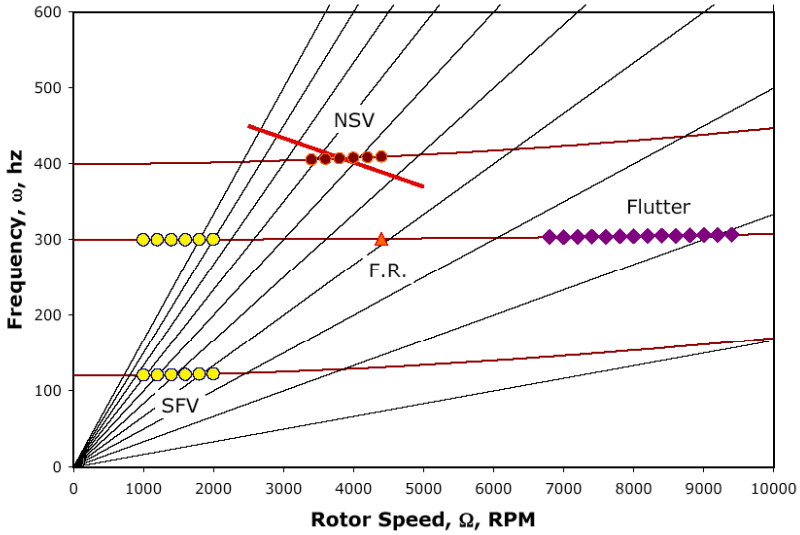

Figure 1. Hypothetical Campbell Diagram Demonstrating Design Considerations Including Non-Synchronous Vibrations (NSV)

As an initial step towards better understanding the NSV in turbine engine configurations, it is advantageous to investigate a well-known two-dimensional case that exhibits similar NSV features such as shedding flow about a circular cylinder. In this case, the flow separates from the cylinder's surface and results in a wake region characterized by a low pressure behind the body (Fox and McDonald 1992, 34). If a cylinder is placed in a low Reynolds number flow (Re>47), vortices are shed alternately from the top and bottom of the cylinder. This phenomenon is generally known as Von Karman vortex shedding.

The flow behind the cylinder becomes three-dimensional for Reynolds numbers greater than 180. This case is much more difficult to model, so this preliminary study only considers flow in the Reynolds number range of $47 < Re < 180$. The Reynolds number measures the relative significance of the viscous effects as compared to inertial

effects. At very low Reynolds number (i.e. Re < 5), the flow remains attached to the cylinder. As the Reynolds number is increased, the flow starts to separate from the surface of the cylinder (5 < Re < 47). At a Reynolds number greater than 47, the flow begins to shed. If the Re is continually increased, the vortices begin to detach themselves from the cylinder, resulting in a periodic wake with two staggered rows of vortices. This regular pattern of vortices is known as a Von Karman vortex street (see Figure 2).

Figure 2. Development of Von Karman Vortex Streets in the Laminar Flow Regime for a Re = 150 (Williamson 2004, 480)

The flow over a stationary cylinder can be determined by two non-dimensional parameters – the Reynolds number and the Strouhal number. For a given Reynolds number, the flow sheds at a distinct frequency. The Reynolds number represents a non-dimensional ratio of the inertial forces in a fluid to the viscous forces. It is given by:

$$\mathrm{Re} = \frac{U_\infty D}{\nu_\infty} \tag{1}$$

where U_∞ is the velocity of the fluid, D is the characteristic dimension (i.e. diameter of the cylinder), and ν_∞ is the kinematic viscosity of the fluid. Whether the flow is laminar or turbulent is primarily governed by the Reynolds number. This study is concerned with the laminar flow over a circular cylinder. Another important parameter related to the

flow over a cylinder is the Strouhal number. This is the non-dimensional vortex shedding frequency. It is:

$$St = \frac{f_{st} D}{U_{\infty}} \tag{2}$$

where f_{st} is the dimensional vortex shedding frequency, D is the cylinder diameter, and U_{∞} is the steady velocity of the uniform flow. A relationship between Reynolds number and Strouhal number was determined.

Another important measure of vortex shedding is the unsteady lift on a stationary cylinder. Lift is primarily due to variations in pressure on the cylinder's surface and is the integrated result of the pressure loading on the cylinder (Norberg 2001, 460). Based on experimental results and 2-D simulations, it can be seen that the amplitude of the RMS lift coefficient increases rapidly within the laminar shedding regime from the onset of shedding at a Reynolds number of 47 (see Figure 10). The onset can be characterized as a supercritical Hopf bifurcation and is typically described by the Stuart-Landau equation (Norberg 2001, 464). The unsteady lift can be used to determine the transition from steady flow to Von Karman vortex shedding in the two-dimensional wake behind a circular cylinder in low Reynolds number flow.

Finally, the HB methodology was applied to both two-dimensional and three-dimensional real world turbomachinery blade applications. Numerous other researchers have studied the NSV problem in turbomachinery and one particular area that has received considerable interest is tip flow instability. Examples of work in this area can be found in Mailach (1999), Mailach et al. (2000 & 2001), Marz et al. (1999 & 2001), Inoue et al. (1999), Lenglin & Tan (2002), and Vo (2001). Mailach et al. (2001) present results from both a four stage low speed research compressor and a linear cascade, and conclude

that the tip flow instability is a vortex interaction effect that produces a multi-cell circumferentially traveling wave. This phenomenon is found near the stall line with a relatively large tip clearance (greater than 2% of tip chord). A new Strouhal-type number is proposed to characterize the frequency of the oscillation. Marz et al. (2001) also found a tip flow instability on a low speed fan rig near the stall line and with a large tip clearance. This paper also presents the results of an unsteady CFD model that predicts a frequency of 950 Hz compared to the measured value of 880 Hz.

Camp (1999) reports that this vexing problem has been observed in a high speed compressor. As a result, an experimental study was performed in a low speed compressor facility. A helical acoustic structure (circumferential Mach number of 0.84) was found using casing dynamic pressure transducers. It was also found that there were step changes in response frequency as the flow rate was changed. Although not proven, the author speculates that the phenomenon involves vortex shedding from the blades that excites the helical acoustic cavity modes, which, in turn, excite the blades.

In this study, we examined three different engine configurations. Based on input from industry, NSV was encountered in experimental rig testing for two of the three test cases. In particular, we studied a modern first stage compressor rotor blade (C1), a modern first stage fan blade (H1), and a modern fan vane blade (H2). Although NSV was not encountered for the H1 case, an analysis was performed to show that NSV is not predicted. As an initial step, a flow instability about a two-dimensional airfoil section of the C1 blade was examined at an off-design condition. Finally, a full three-dimensional analysis of all three blades was performed to predict both the frequency and amplitude of the fluid dynamic instability.

2. THEORY

In general, the unsteady perturbations are significant and serve as a useful test case for the verification of the harmonic balance method as a valuable tool for solving NSV problems in turbomachinery. The flow over the cylinder is modeled by the two-dimensional nonlinear, unsteady Navier-Stokes equations. Two currently available analysis techniques, namely the time domain approach and the time-linearized frequency domain approach, were considered and the merits of each were examined. Finally, the harmonic balance method developed by Kenneth Hall will be described. For time-periodic flows, Hall's method can be computationally more efficient than the other approaches and it is not limited by the assumptions required by a linearized solution.

In the past, most researchers have employed a time-domain approach to model the fluid flow over bluff bodies (Ni 1987, He 1993). In this case, the governing Navier-Stokes equations are discretized over the computational grid and then the flow solution is marched in time using conventional CFD techniques and applying appropriate unsteady boundary conditions. The discretization of the flow equations requires the solution of a set of coupled nonlinear equations at each physical time step. Commonly, an inner iteration is introduced with a pseudotime variable and marched to a steady state. The converged solutions obtained at the end of the inner iteration represents a solution of the equations at the end of the physical time step (McMullen, Jameson, and Alonso 2001, 1). Therefore, this procedure must be repeated numerous times to achieve one physical time step and resolve the features of one period in the oscillation of the flow. Many convergence acceleration techniques such as multi-grid and variable pseudotime stepping can be implemented in the inner iteration. However, as more periods are needed for

convergence, the computations can become extremely costly. Although this approach is straightforward to implement and can model both nonlinear as well as linear disturbances, it typically takes considerable computational time to ensure numerical stability. Therefore, this approach is too expensive for routine use by industry to predict and design for NSV.

Another popular technique for modeling the flow over turbomachinery blades is the time-linearized frequency domain approach. This method has been used to model transonic flow problems as well as two- and three-dimensional viscous flows in turbomachinery (Clark and Hall 2000, Hall and Crawley 1989). In this method, the problem is divided into two parts: the steady flow and the unsteady perturbations in the flow. The steady, or time-mean, part of the flow is solved using well-known CFD techniques and the unsteady part is assumed to be small and harmonic in time ($e^{j\omega t}$). The governing Navier-Stokes equations can then be linearized about the mean flow solution to determine a set of equations that describe the unsteady flow component and they can be solved relatively easily. By replacing the time derivative by $j\omega$ where ω is the frequency of the unsteady flow disturbance, the resulting time-linearized equations can be solved inexpensively. A solution to the complex harmonic amplitude is obtained at a given frequency. When compared to unsteady time marching methods, the time-linearized frequency domain method is much more efficient but it is limited by the linear assumption of unsteadiness.

This study utilizes the harmonic balance technique for nonlinear, unsteady flows developed at Duke University by Kenneth Hall in 2002. It was originally developed as a mathematical tool to study the behavior of harmonic ordinary differential equations

(Maple 2002, 3). However, in recent years, Hall extended the application to the study of turbomachinery flows. In this novel method, the unsteady flow is assumed to be periodic time and can be represented by a Fourier series in time with frequencies that are integer multiples of the fundamental excitation frequency. Then, using the harmonic balance technique, a set of coupled partial differential equations is obtained for the unknown Fourier coefficients of the flowfield. A source term, dU/dt, accounts for the unsteadiness. Finally, a pseudo-time term is introduced into the harmonic balance equations and the solution is marched like a steady CFD solver. From this result, the lift, drag, etc. for each harmonic can be determined from the calculated Fourier coefficients. For a given problem, it is desirable to use the minimum number of harmonics because the computational cost is proportional to the number of harmonics included. Local time stepping, preconditioning, and multi-grid can be use to accelerate convergence. Therefore, a key aspect of the methodology is its ability to exploit the use of conventional CFD techniques. The theory presented in Hall's paper entitled, "Computation of Unsteady Flow in Cascades Using a Harmonic Balance Technique", is summarized in the following sections.

Governing Equations

The flow over a cylinder can be best represented by the Reynolds-averaged, two-dimensional Navier-Stokes equations for unsteady, nonlinear flow. The derivation of these equations is well documented in literature and arises from applying three conservation laws: conservation of mass, conservation of momentum, and conservation of energy (Anderson 1984, 181). The flow is assumed to be compressible and viscous. Therefore, the resulting equations of motion in integral form are:

$$\frac{d}{dt}\iint_{D_c} U dxdy + \oint_{\partial D_c}(F - U\frac{\partial f}{\partial t})dy - \oint_{\partial D_c}(G - U\frac{\partial g}{\partial t})dx = \iint_{D_c} S dxdy \tag{3}$$

where D_c is a deforming control volume bounded by the control surface ∂D_c. U is a vector of conservation variables, F and G are flux vectors in the x and y directions, and S is the source vector. The quantities $\partial f/\partial t$ and $\partial g/\partial t$ are the x and y components of the velocity of the control surface ∂D_c. Based on the strong conservative law form of the Navier-Stokes equations given above, the vector U and the inviscid and viscous components of F, G and S can be written in vector form as:

$$U = \begin{bmatrix} \rho \\ \rho u \\ \rho v \\ \rho e \end{bmatrix}, \qquad F = \begin{bmatrix} \rho u \\ \rho u^2 + p - \tau_{xx} \\ \rho uv - \tau_{xy} \\ \rho uh - \tau_{hx} \end{bmatrix}, \tag{4}$$

$$G = \begin{bmatrix} \rho v \\ \rho uv - \tau_{xy} \\ \rho v^2 + p - \tau_{yy} \\ \rho vh - \tau_{hy} \end{bmatrix}, \qquad S = \begin{bmatrix} 0 \\ 0 \\ 0 \\ 0 \end{bmatrix}$$

By examining the governing equations in compact vector form, the first row corresponds to the continuity equation, the second and third rows are the momentum equation in the x and y directions respectively, and the final equation is the conservation of energy equation. In these equations, ρ is the density of the fluid; u and v are the velocity components in the x and y directions, respectively; e is the total internal energy; h is the total enthalpy; and p is the static pressure. If the divergence theorem is applied, a differential form of the Navier-Stokes is obtained:

$$\frac{\partial U}{\partial t} + \frac{\partial F(U)}{\partial x} + \frac{\partial G(U)}{\partial y} = S \tag{5}$$

Assuming the fluid (air in this case) is an ideal gas with constant specific heats, it is possible to express the pressure and enthalpy in terms of the conservation variables. The equation of state is given by:

$$p = \rho RT \tag{6}$$

where T is the temperature and R is the universal gas constant. In addition, for a perfect gas, the following relationships exist:

$$e = c_v T, \quad h = c_p T, \quad \gamma = \frac{c_p}{c_v}, \quad c_v = \frac{R}{\gamma - 1}, \quad c_p = \frac{\gamma R}{\gamma - 1} \tag{7}$$

where c_v is the specific heat at constant volume, c_p is the specific heat at constant pressure, and γ is defined as the ratio of these two specific heats. Therefore, the pressure and enthalpy can be determined and are given by:

$$p = (\gamma - 1)\{\rho e - 1/2\rho[(\rho u)^2 + (\rho v)^2]\} \tag{8}$$

$$h = (\rho e + p)/\rho \tag{9}$$

The shear stresses τ_{xx}, τ_{xy}, τ_{yy} can be written in terms of the viscosity and the shear rate in the x and y directions, respectively:

$$\tau_{xx} = \mu\left(\frac{4}{3}\frac{\partial u}{\partial x} - \frac{2}{3}\frac{\partial v}{\partial y}\right) \tag{10}$$

$$\tau_{xy} = \mu\left(\frac{\partial u}{\partial y} + \frac{\partial v}{\partial x}\right) \tag{11}$$

$$\tau_{yy} = \mu\left(\frac{4}{3}\frac{\partial v}{\partial y} - \frac{2}{3}\frac{\partial u}{\partial x}\right) \tag{12}$$

where μ is the molecular viscosity. Furthermore, the terms τ_{hx} and τ_{hy} in the energy equation are given by:

$$\tau_{hx} = u\tau_{xx} + v\tau_{xy} - q_x \tag{13}$$

$$\tau_{hy} = u\tau_{xy} + v\tau_{yy} - q_y \tag{14}$$

where q_x and q_y are the x and y components of the heat flux and can be written as:

$$q_x = -\left(\frac{\mu c_p}{\mathrm{Pr}_L}\right)\frac{\partial T}{\partial x} \tag{15}$$

$$q_y = -\left(\frac{\mu c_p}{\mathrm{Pr}_L}\right)\frac{\partial T}{\partial y} \tag{16}$$

where Pr_L is the laminar Prandtl number and $\partial T/\partial x$ and $\partial T/\partial y$ are the temperature gradients in the x and y directions, respectively. The variable μ is determined from Sutherland's Law and results from the use of a dynamic molecular viscosity. Sutherland's formula for viscosity is given by:

$$\mu = \mu_0 (T/T_0)^{3/2}\left(\frac{T + S_0}{T_0 + S_0}\right) \tag{17}$$

where $\mu_0 = 3.583 \times 10^{-7}$ at a reference temperature $T_0 = 491.4°R$ and the constant $S_0 = 199.8°R$. For air at standard conditions, $\mathrm{Pr_L} = 0.72$. Therefore, by using knowledge of the flow and the principles of thermodynamics, it is now possible to implement the harmonic balance method to solve the governing two-dimensional, nonlinear, unsteady Navier-Stokes equations.

Non-Dimensionalization

In order to make the computations easier, the equations are often put into a non-dimensional form. This allows the system parameters such as Reynolds number, Mach number, etc. to be varied independently (Anderson 1984, 191). Therefore, the variables of interest were non-dimensionalized as follows:

$$x' = \frac{x}{L_{ref}},\ y' = \frac{y}{L_{ref}},\ u' = \frac{u}{V_{ref}},\ v' = \frac{v}{V_{ref}}, \tag{18}$$

$$p' = \frac{p}{p_{ref}},\ T' = \frac{T}{T_{ref}},\ \rho' = \frac{\rho}{\rho_{ref}},\ \mu' = \frac{\mu}{\mu_{ref}}$$

where the reference quantities are given by:

L_{ref}	is a user-defined constant length scale
p_{ref}	is the user-defined total pressure
T_{ref}	is the user defined total temperature
ρ_{ref}	is the total density defined as $\rho_{ref} = p_{ref}/R_{ref}T_{ref}$
a_{ref}	is the freestream total acoustic velocity defined as $a_{ref} = (\gamma R_{ref}T_{ref})^{1/2}$
V_{ref}	is the reference velocity defined as $a_{ref}/(\gamma)^{1/2}$
μ_{ref}	is the reference viscosity defined as $\mu_{ref} = \rho_{ref}\nu_{ref}L_{ref}$

By rewriting the equations in dimensionless form, it makes it easier to compare with experimental results. As a result, the system's behavior and dependence on various parameters can be extracted more easily.

Application of Harmonic Balance Method to Governing Equations

To introduce the harmonic balance method in a simplistic manner, one can assume that the flow is inviscid and non-heat conducting, as was done by Hall, et al. in 2002 (Hall, Thomas, and Clark, 879-886). In his paper, the flow was modeled by the two-dimensional Euler equations:

$$\frac{\partial U}{\partial t} + \frac{\partial F(U)}{\partial x} + \frac{\partial G(U)}{\partial y} = 0 \tag{19}$$

where the vector of conservation variables and the flux vectors F and G are given by:

$$U = \begin{bmatrix} \rho \\ \rho u \\ \rho v \\ \rho e \end{bmatrix}, \quad F = \begin{bmatrix} \rho u \\ \rho u^2 + p \\ \rho uv \\ \rho uh \end{bmatrix}, \quad G = \begin{bmatrix} \rho v \\ \rho uv \\ \rho v^2 + p \\ \rho vh \end{bmatrix} \tag{20}$$

To begin the analysis, one first assumes that the flow behind the cylinder is temporally periodic whereby,

$$U(x, y, t) = U(x, y, t + T) \tag{21}$$

where T is the period of the unsteadiness and is given by $T = 2\pi/\omega$. Here, ω is the frequency of the unsteadiness. As result of the temporal periodicity of the flow, the flow variables can be represented as a Fourier series in time with spatially varying coefficients. Therefore, the density becomes:

$$\rho(x, y, t) = \sum_n R_n(x, y) e^{j\omega n t} \tag{22}$$

Similar relationships can be obtained for the other conservation variables as well as $1/\rho$, which is necessary for determining the enthalpy and pressure. In theory, one would sum the variables over all *n* but in practice, the solution is truncated and summed over a finite number of terms. Next, the Fourier expansions are substituted into the Euler equations and expressions for the conservation of mass, momentum, and energy can be developed. The terms in the resulting equations are grouped by frequency and each frequency component must satisfy the conservation equations individually. The equations can then be written in vector form as:

$$\frac{\partial \tilde{F}(\tilde{U})}{\partial x} + \frac{\partial \tilde{G}(\tilde{U})}{\partial y} + \tilde{S}(\tilde{U}) = 0 \tag{23}$$

where the tilde indicates a Fourier transformed variable and $\tilde{S}$ is the frequency component resulting from the transformed time dependent variable $\partial U/\partial t$. In addition, since the conservation variables are all real-valued, it is only necessary to store the Fourier coefficients for non-negative n. For example, if N_H harmonics are retained in the Fourier series, then $2N_H + 1$ coefficients must be stored for each flow variable. There is one for the zeroth harmonic (mean flow) and $2N_H$ for the real and imaginary components of the rest of the harmonics (Hall, Thomas, and Clark 2002, 881). However, this method

proved to be extremely difficult and computationally expensive so an alternate approach was developed to reduce the complexity of the problem.

Utilization of Time Domain Methodology

The new method works in terms of time domain variables by assuming that the values of *U*, *F*, and *G* could be evaluated at $2N_H+1$ equally spaced points in time over one temporal period. Therefore,

$$U^* = E^{-1}\tilde{U} \tag{24}$$

where U^* is a vector of the conservation variable evaluated at $2N_H+1$ points and E^{-1} is the inverse discrete Fourier transform operator. Similar expressions can be developed for the flux vectors and the new governing vector equation becomes:

$$\frac{\partial F^*}{\partial x} + \frac{\partial G^*}{\partial y} + S^* = 0 \tag{25}$$

where

$$S^* = j\omega E^{-1} N E U^* \approx \frac{\partial U^*}{\partial t} \tag{26}$$

S^* is a spectral operator which approximates the change in U^* with respect to time. This method can easily be extended to the two-dimensional, unsteady, viscous Navier-Stokes equations used in this study. The technique used to actually solve the governing equations will be described in the next section.

Numerical Solution Technique

To obtain the solution to the harmonic balance equations, a pseudotime term was introduced. This allows the equations to be marched to a steady state using conventional CFD techniques. For the Euler equations, the equation becomes:

$$\frac{\partial U^*}{\partial \tau} + \frac{\partial F^*}{\partial x} + \frac{\partial G^*}{\partial y} + S^* = 0 \tag{27}$$

where τ is a new time variable merely used to march the equation to a steady state. This equation very closely resembles the differential form of the Euler equations so it is analogous to solving the time domain equations using a CFD scheme. Therefore, the overall method would consist of pseudotime marching N x $(2N_H + 1)$ dependent variables, where N is the number of mesh points and N_H is the number of harmonics retained in the solution.

Grid Generation

In general, the grid is constructed based on the geometric attributes of the body under consideration. The flow properties at each point in the grid are assigned a value based on the initial flow condition (Ni 1982, 1565). Then, the governing equations are discretized into distinct cells on a computational mesh. The solution is then numerically integrated for each cell over the entire domain. Finally, the governing equations are marched in the psuedo time domain. Multi-grid and local time stepping methods can be used to accelerate convergence. Effectively, multi-grid uses a combination of fine grids and coarse grids to achieve both rapid solution convergence as well as accuracy.

Lax-Wendroff Method

In particular, for the two-dimension Navier-Stokes equations, a computational grid is generated for each time level and then the harmonic balance equations are discretized over the entire domain using common CFD techniques. The conservation variables are stored at each node of the grid for each time level. In this analysis, the two-step Lax-Wendroff method was used to solve the harmonic balance equations. The Lax-Wendroff method is a node-centered conservative finite difference scheme. For the

Navier-Stokes equations, the Lax-Wendroff scheme is second-order accurate in space and first order accurate in time due to viscous terms (Davis, Ni, and Carter 1987, 407). As before, the Navier-Stokes equations are given as:

$$\frac{\partial U}{\partial t} + \frac{\partial F}{\partial x} + \frac{\partial G}{\partial y} = S \tag{28}$$

where *U*, *F*, *G*, and *S* are defined in the preceding section. The Lax-Wendroff method is developed from a Taylor series expansion of *U* in time:

$$U(x, y, t + \Delta t) = U(x, y) + \Delta t \frac{\partial U(x, y)}{\partial t} + \left(\frac{\Delta t^2}{2} \right) \frac{\partial^2 U(x, y)}{\partial t^2} + O(\Delta t^3) \tag{29}$$

The first derivative term can be determined from the governing equation and therefore can be written as:

$$\frac{\partial U}{\partial t} = -\left[\frac{\partial F}{\partial x} + \frac{\partial G}{\partial y} \right] + S \tag{30}$$

The second time derivative can be found by differentiating this equation with respect to time:

$$\frac{\partial^2 U}{\partial t^2} = -\left[\frac{\partial}{\partial x} \left(\frac{\partial F}{\partial U} \right) \left(\frac{\partial U}{\partial t} \right) + \frac{\partial}{\partial y} \left(\frac{\partial G}{\partial U} \right) \left(\frac{\partial U}{\partial t} \right) \right] + \left(\frac{\partial S}{\partial U} \right) \left(\frac{\partial U}{\partial t} \right) \tag{31}$$

When these expressions are substituted back into the Taylor-series expansion for U, the resulting equation becomes:

$$U(x, y, t + \Delta t) = U(x, y) - \Delta t \left[\left(\frac{\partial F}{\partial x} + \frac{\partial G}{\partial y} \right) - S \right] - \left(\frac{\Delta t^2}{2} \right) \left[\frac{\partial \Delta F}{\partial x} + \frac{\partial \Delta G}{\partial y} - \Delta S \right] + O(\Delta t^3) \tag{32}$$

where $\Delta U = (\partial U/\partial t)\Delta t$, $\Delta F = (\partial F/\partial U)\Delta U$, $\Delta G = (\partial G/\partial U)\Delta U$, $\Delta H = (\partial H/\partial U)\Delta U$, and $\Delta S = (\partial S/\partial U)\Delta U$.

Therefore, the first derivative representation provides a first-order correction whereas the second derivative gives a second-order correction. This technique is applied to the harmonic balance described in the previous section and the solution can be obtained by marching these equations in time at each grid point. A steady state is reached when the corrections are driven to zero. Since this method was originally developed for inviscid flow analysis, some small changes must be made to the integration scheme to handle the viscous components (Davis, Ni, and Carter, 409). Finally, it is common to use an artificial viscosity to maintain stability in regions with large discontinuities and coarse grid spacing. In this study, both second and fourth difference numerical smoothing are used to eliminate oscillations.

Application of Initial and Boundary Conditions

In addition, proper boundary and initial conditions must be applied. In particular, at each iteration of the code, the no-slip boundary condition must be applied on the cylinder surface since viscous flow analysis is being conducted. Furthermore, the periodicity conditions must be implemented. Also, non-reflecting far field boundary conditions should be applied in the frequency domain such that there are no disturbances far from the body (Hall, Thomas, and Clark 2002, 882). Finally, both upstream and downstream initial flow conditions are prescribed.

Frequency Search Procedure

Once the system has been completely described, CFD techniques can be invoked and the equations are marched in pseudo-time until convergence is reached. However, nonlinear harmonic balance analysis requires the user to input the frequency of the flow instability (a known quantity) to the system. Since the purpose of the study is to find the

NSV frequency, two different approaches can be applied. A simple method is to choose a wide range of frequencies and compute the solution residual of the harmonic balance equation for each case. The NSV frequency corresponds to that for which the harmonic balance solution residual goes to zero. However, previous studies by McMullen, et al. indicate the solution residual drops off suddenly at the precise NSV frequency (McMullen, Jameson, and Alonso 2002, 6). As a result, this method of guessing frequencies can easily miss the correct NSV frequency and also requires numerous iterations of the harmonic balance code.

Phase Error Method

Therefore, a novel frequency search technique was developed by Hall (private communication). This technique requires much fewer harmonic balance calculations than the frequency sweep method. For a given frequency, the converged solution will have a constant amplitude and phase. The phase shift can be calculated relatively simply once the unsteady lift is determined. After each iteration of the HB solver, the phase is updated and the change in phase from one iteration to the next is computed. When an incorrect frequency is inputted using the nonlinear harmonic balance method, it was discovered that the amplitude of any unsteady first harmonic quantity, such as unsteady lift, stays nearly constant but the phases rotates from one iteration to the next and eventually settles down to constant value. Once this value is calculated for a couple different frequencies, it becomes readily apparent that the phase is nearly linearly related to the frequency. The exact frequency can be calculated by determining the frequency for which the phase shift is zero. This can be accomplished by simple interpolation.

Thus, this simple phase error technique results in a reasonable approximation of the NSV frequency and only requires a few harmonic balance calculations.

3. APPLICATIONS OF HARMONIC BALANCE METHOD

3.1 STATIONARY CYLINDER IN CROSS FLOW

A well-studied fluid dynamics phenomenon is a stationary cylindrical structure in cross flow. This test case is important for the study of towers, cables, antennae, wires, etc. As a result, extensive experimental data is available demonstrating the relationship between Strouhal number and Reynolds number. Therefore, as an initial illustration of the merits of the harmonic balance method, the first goal was to reproduce these experimentally determined results. The problem was modeled using the HB method and a 129x65 mesh for various Reynolds numbers. A typical mesh is shown in Figure 3 with 129 points in the circumferential direction and 65 points in the radial direction. The mesh boundary is 40 diameters from the center of the cylinder in this figure.

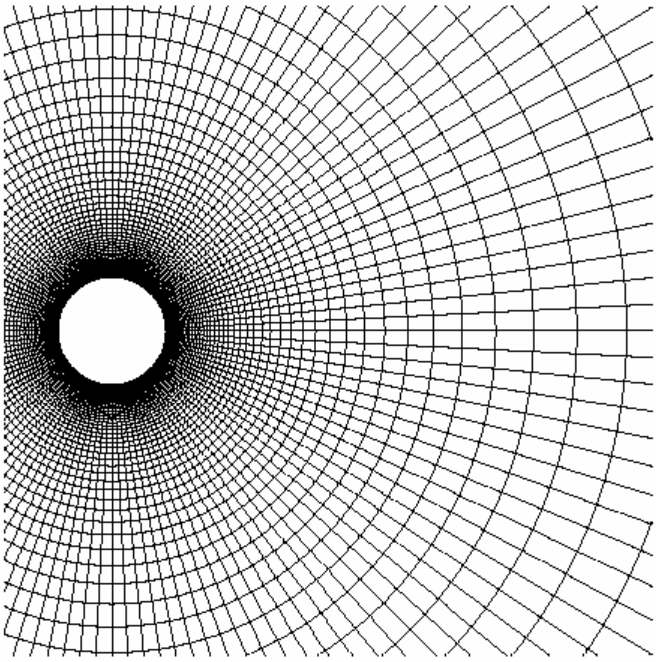

Figure 3. Computational Grid (129x65 mesh) for Cylinder in Cross Flow

Application of Phase Error Method

To determine the Strouhal number representing the NSV frequency for a particular Reynolds number, it was necessary to run the code for different Strouhal numbers and note the solution residual for each case. Figure 4 shows the HB solution residuals for a number of assumed Strouhal numbers at a Reynolds number of 170 using two harmonics. As can be seen from the graph, the predicted Strouhal number is approximately 0.1865. The NSV frequency or the "correct" frequency is that for which the solution residual drops down significantly i.e. |dq| = |0| (the difference between the current solution and the previous solution is zero). However, this method requires the user to run the code for many different cases to hone in on the precise NSV frequency.

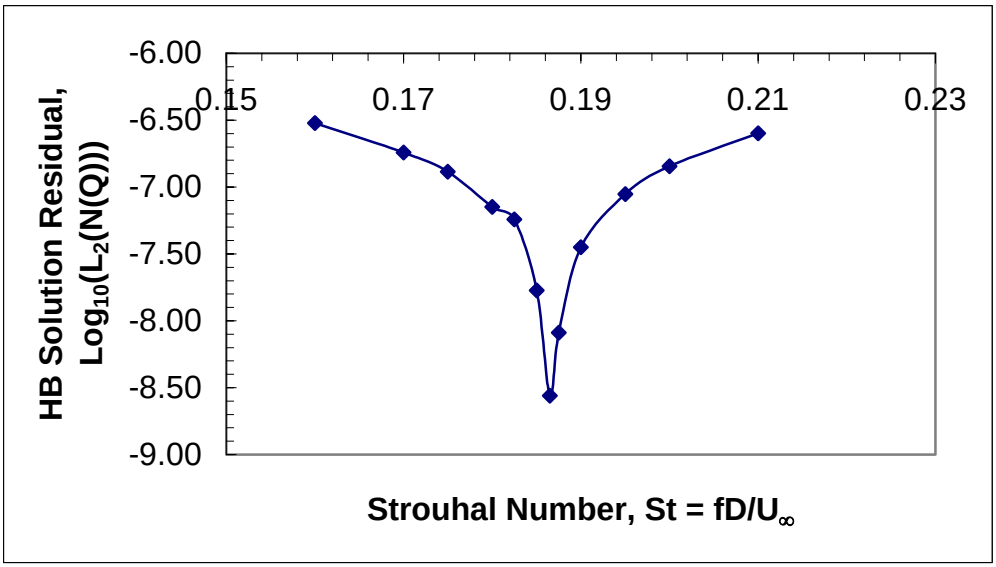

Figure 4. HB Solution Residual versus Strouhal Number – Re = 170 (2 Harmonics)

A more efficient method is to use the phase error method described previously that utilizes the change in an integrated global quantity such as the phase of the unsteady lift as opposed to the solution residual. By choosing the same Strouhal numbers, the phase shift per iteration was also determined. A plot of these quantities is shown in Figure 5 and it can be seen that the change in phase of the unsteady lift is nearly linear

with respect to the Strouhal number. The zero crossing represents the NSV non-dimensional frequency and is also the point where the HB solution residual exhibits a sudden drop-off. Therefore, it is only necessary to run the code for a small number of different frequencies and note the change in phase of the unsteady lift for each case. Then, one can interpolate between these points to find the zero crossing, which corresponds to the precise NSV frequency. Therefore, this frequency search technique provides a solution much more quickly than simply searching directly for the frequency where the HB solution residual is a minimum. Furthermore, a more accurate solution can be obtained by adding more harmonics and performing a mesh refinement study.

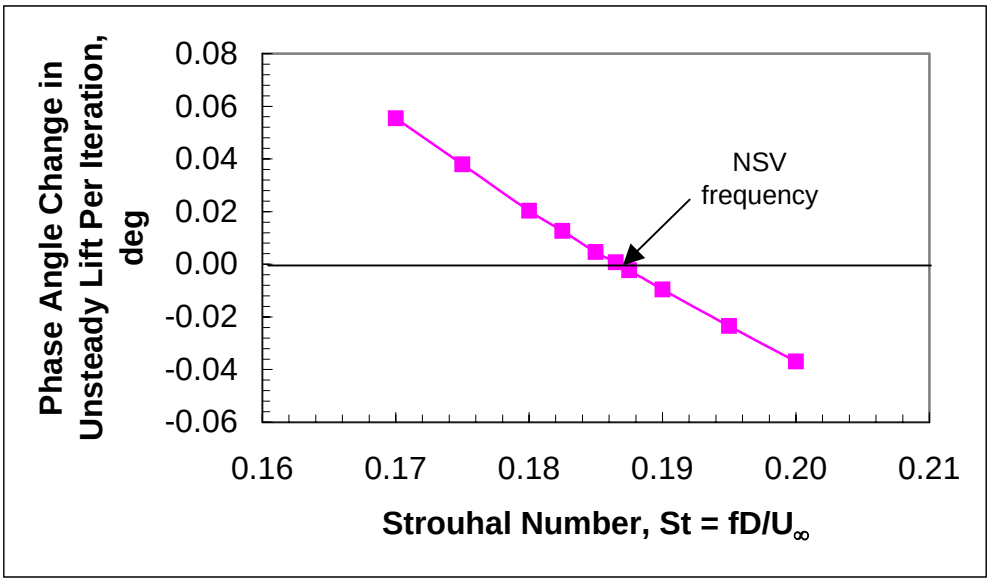

Figure 5. Change in Phase Angle of Unsteady Lift Per Iteration – Re = 170 (2 Harmonics)

Strouhal – Reynolds Number Relationship

This process was repeated for a range of Reynolds numbers in the laminar flow regime and a corresponding Strouhal number was determined for each case. The resulting Strouhal numbers were then compared with experimental data collected by Williamson in 1996 (Williamson, 494). The results can be found in Figure 6.

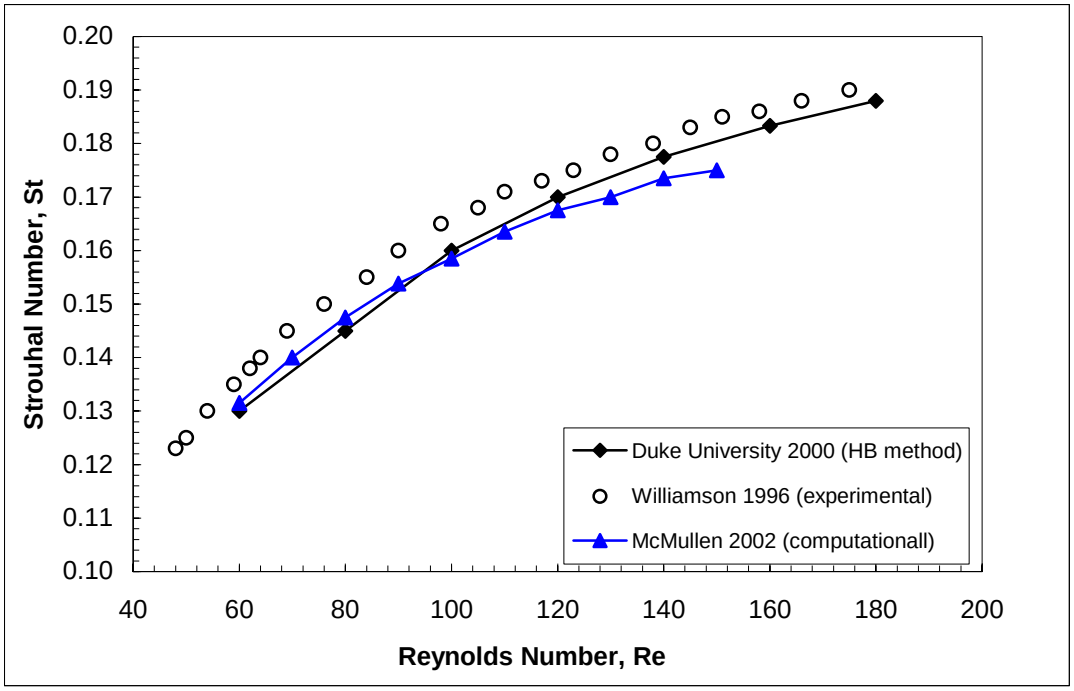

Figure 6. Cylinder in Cross Flow - Strouhal Number Dependency on Reynolds Number

As can be seen from the plot, the HB method shows good agreement with the experimentally determined values. Previous studies had indicated large discrepancies in the St –Re relationship in the laminar flow region but Williamson found that the wake frequency was very sensitive to the experimental setup, particularly the 3-D effects of oblique vortex shedding. To counter these effects, parallel shedding was induced by angling the endplates on the cylinder (Williamson 1988, 2744). Therefore, by applying this end boundary condition and ensuring the freestream is sufficiently uniform, a curve is produced that is universal as well as continuous. Therefore, the harmonic balance method accurately predicts the relationship between Strouhal number and Reynolds number.

Stationary Cylinder Flow Simulation

A typical flow solution for the total pressure contours for Reynolds numbers of 50, 100, and 170 are shown in Figures 7, 8, and 9, respectively. These plots demonstrate the low-pressure region that is generated behind the cylinder and also show the formation of vortices in the cylinder's wake. In particular, for Re = 50, it shows the beginning of the vortices being shed alternatively from the top and bottom of the cylinder. For Reynolds numbers of 100 and 170, the wake has become unstable and the vortices have detached themselves from the cylinder. Consequently, staggered rows of vortices of opposite sign are being formed. Therefore, the HB method is able to produce time accurate results and is a viable tool to predict the frequency of the unsteady flow about a stationary cylinder in cross flow and the solution at chosen Reynolds numbers agrees well with previous experimental investigations. Furthermore, the observed flow patterns, such as the Von Karman vortex street, are consistent with previous experimental flow simulation results. This can be seen by comparing the figures below with Williamson's photograph of the formation of Von Karman vortex streets in the introduction.

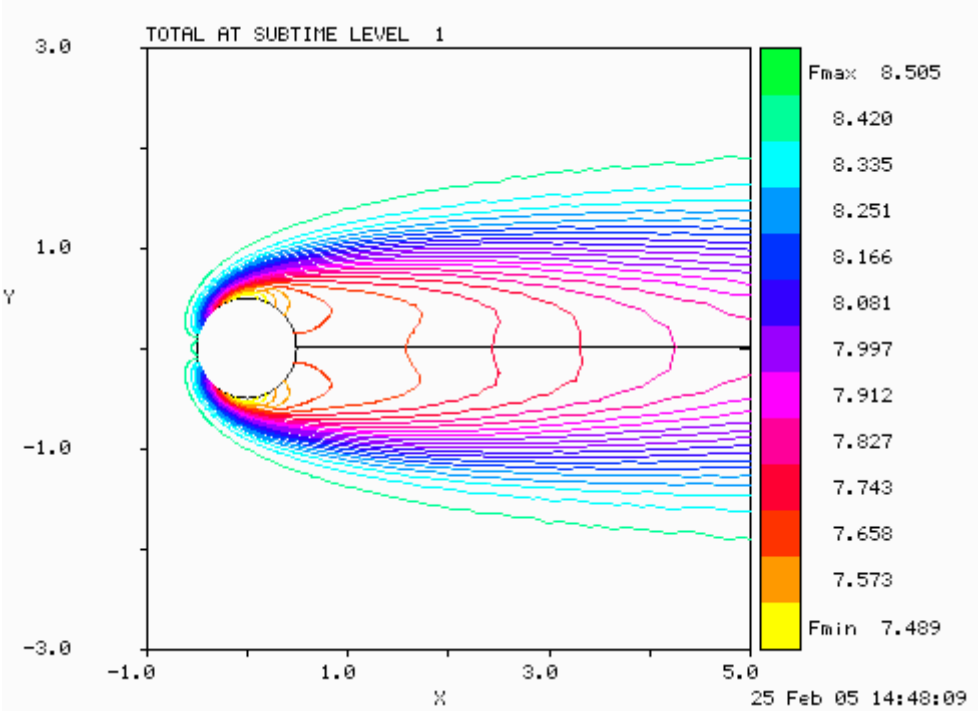

Figure 7. Total Pressure Contours for Flow Over a Cylinder at Re = 50

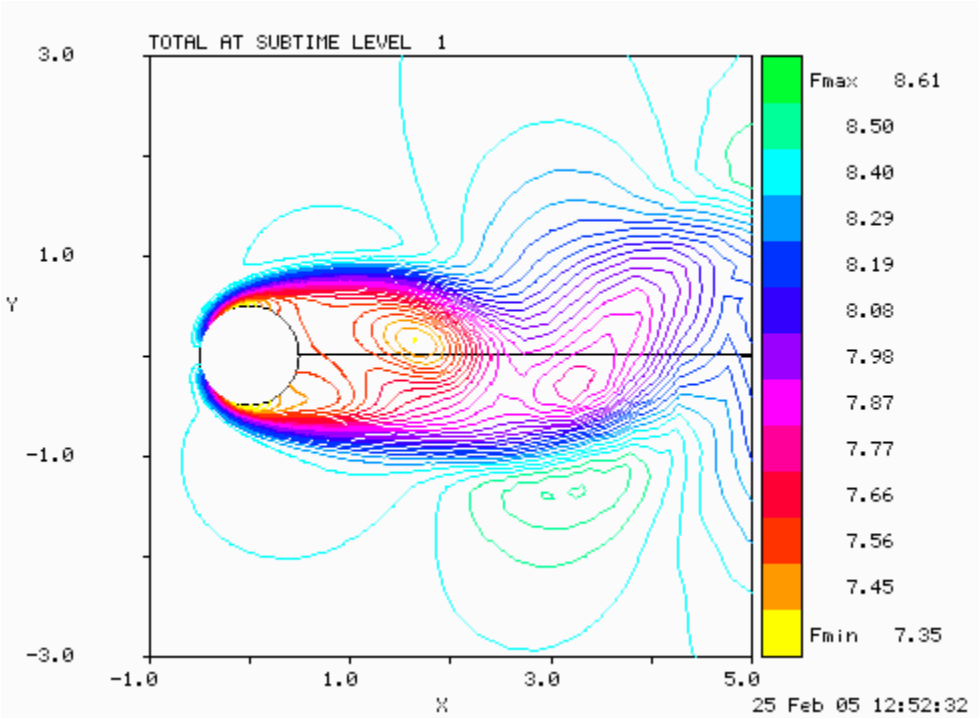

Figure 8. Total Pressure Contours for Flow Over a Cylinder at Re = 100

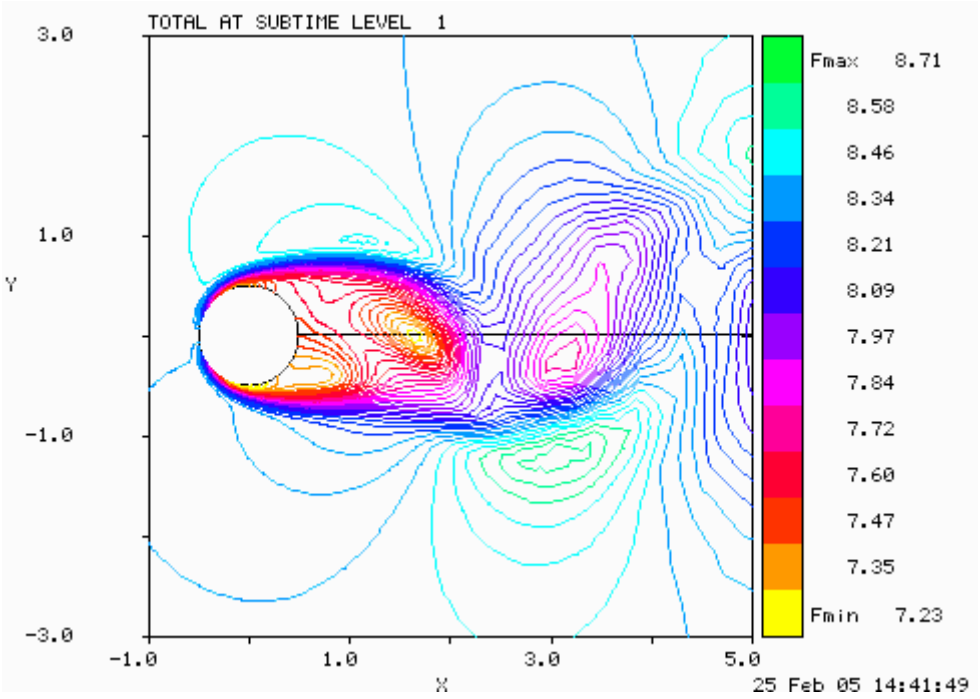

Figure 9. Total Pressure Contours for Flow Over a Cylinder at Re = 170

Unsteady Cylinder Lift

In addition to determining the frequency of the fluid dynamic instability, another important quantity to be able to calculate is the RMS amplitude of the lift on the cylinder. At the NSV frequency for a range of Reynolds numbers, the amplitude of the first harmonic lift acting on the shedding cylinder is determined. A plot demonstrating this relationship can be found in Figure 10. This plot gives a measure of the unsteady lift (1^{st} harmonic). The alternate periodic shedding causes the pressure fluctuations at around f_{st} to be essentially out-of-phase between the upper and lower side of the cylinder so the lift fluctuation energy is concentrated to a band around f_{st} (Norberg 2003, 57). Furthermore, by extrapolating to the Reynolds number of zero oscillating lift, the onset of the vortex shedding can be determined. Figure 10 shows that this occurs at about a Reynolds number of 47, which is approximately the same as the value determined from nonlinear dynamic numerical techniques (Norberg 2001, 464). In addition, the plot shows that

there is rapid increase in the unsteady RMS lift coefficient within the laminar shedding regime. This is characteristic of all supercritical Hopf bifurcations in which the size of the limit cycle grows continuously from zero, and increases proportional to $(\mu - \mu_c)^{1/2}$ where μ is a control parameter. In fact, experimental studies and 2-D simulations have shown that the unsteady lift coefficient exhibits this square-root dependency on Reynolds number, $C_{L'} \propto \varepsilon = (Re-Re_c)/Re_c))^{1/2}$ where Re_c is the critical Reynolds number for which shedding begins (Norberg 2001, 464). Therefore, by examining the nonlinear dynamics of the system, the unsteady lift provides a measure of the stability of the system and can be used to determine the transition from steady flow to Von Karman vortex shedding in the 2-D cylinder wake. Furthermore, the HB method demonstrates the unsteady lift's square-root dependency on Reynolds number.

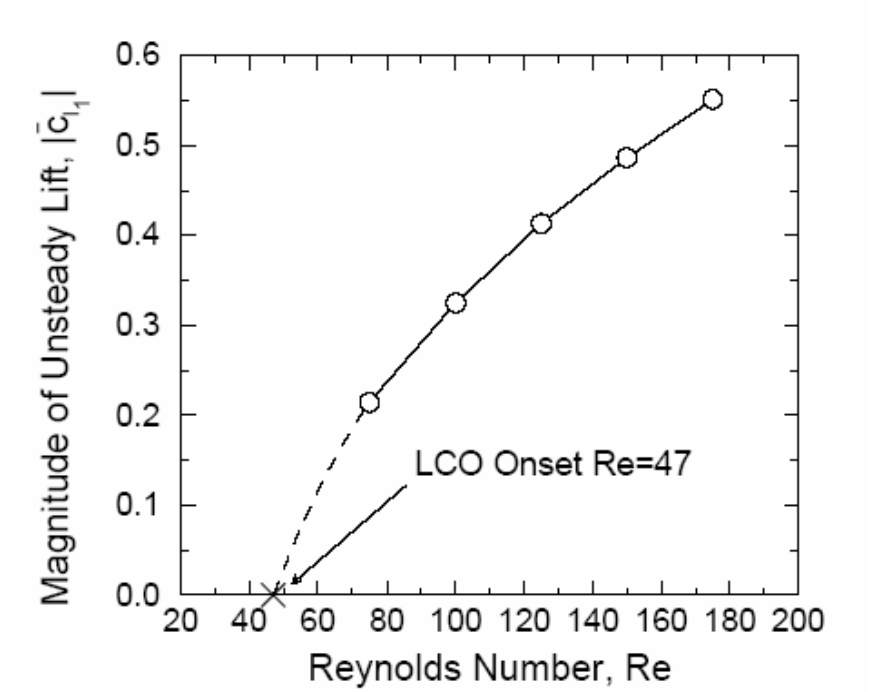

Figure 10. Computed Amplitude of First Harmonic of Unsteady Lift Acting on Shedding Cylinder from Onset at Re = 47

Experimental Procedure and Results

To validate the results obtained by the HB method, a comparison was made with the experimental study of Tanida, et al. as well as numerous 2-D numerical simulations. Figure 11 shows that the results obtained from the HB method show reasonable agreement with the 2-D computational data but vary considerably from the experimental data. This discrepancy may be explained in part by the use of unsealed gaps in Tanida's towing tank study (Norberg 2003, 65). Tanida, et al. utilized a force element method to measure the fluctuating lift in which the load-transmitting part of the cylinder is connected to a cantilever beam element that is fixed to a base inside a "dummy" part of the cylinder. Keefe found that unsealed gaps can result in a drastic reduction in fluctuating unsteady lift forces as Reynolds number is decreased, as much as 10 times lower than with sealing (Keefe 1962, 1712). However, his experiment was conducted at higher Reynolds number so it is difficult to determine a definitive reason for the incongruity between the experimental and computational data. Unfortunately, this is the only experimental data available in the Reynolds regime of interest so it is hard to make a qualitative comparison. When the HB method is compared with other numerical simulations, it seems to slightly over predict the unsteady lift coefficient. As a result, further study is required to determine the validity of Tanida's experimental results.

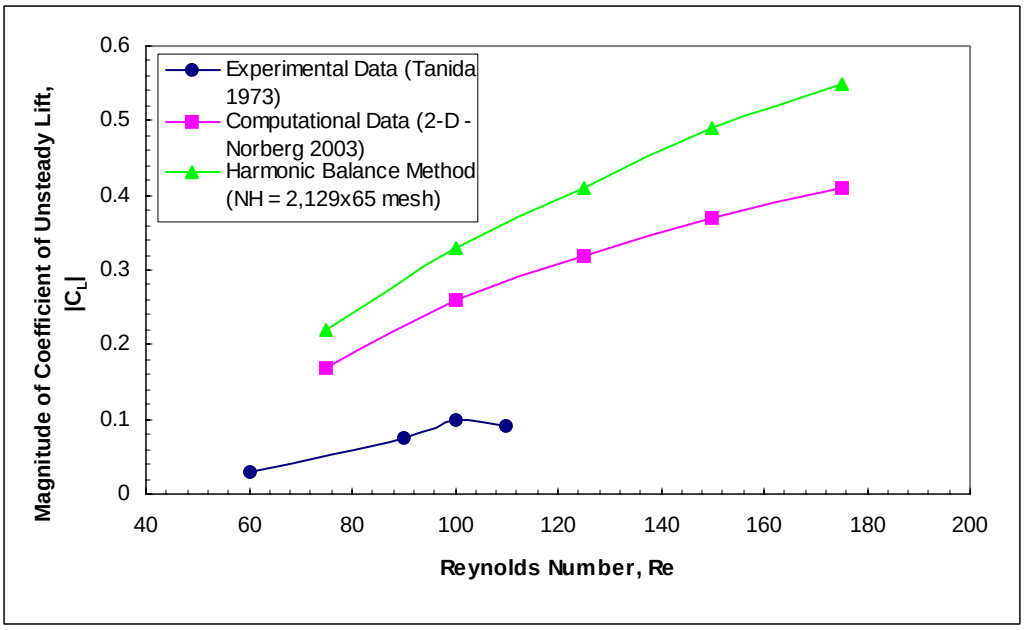

Figure 11. Comparison of Lift Data with Other Numerical Results and Experimental Data

Mean Cylinder Drag

Another interesting feature to examine is the response of the cylinder drag to the onset of unsteadiness and vortex shedding. There are numerous contributions to the total drag on a cylinder, including the viscous drag coefficient and the pressure drag coefficient. Henderson computed these coefficients numerically using a highly accurate spectral element method based on 8th order polynomials (Henderson 1995, 2102). Furthermore, McMullen also computed the drag forces as a function of Reynolds number using a frequency domain technique. The change from a steady to an unsteady wake is marked by a gradual decrease in the viscous drag coefficient as well as the total drag throughout the laminar flow regime (Henderson 1995, 2103). A plot comparing the values obtained by Henderson, McMullen, and the harmonic balance method is found in Figure 12. The results from the harmonic balance method are very similar to those obtained by both Henderson and McMullen. It is noted that the mean drag coefficients

are relatively constant with respect to Reynolds number as compared to the lift coefficients. Therefore, the harmonic balance method is further validated as a valuable tool for predicting the forces on a cylinder.

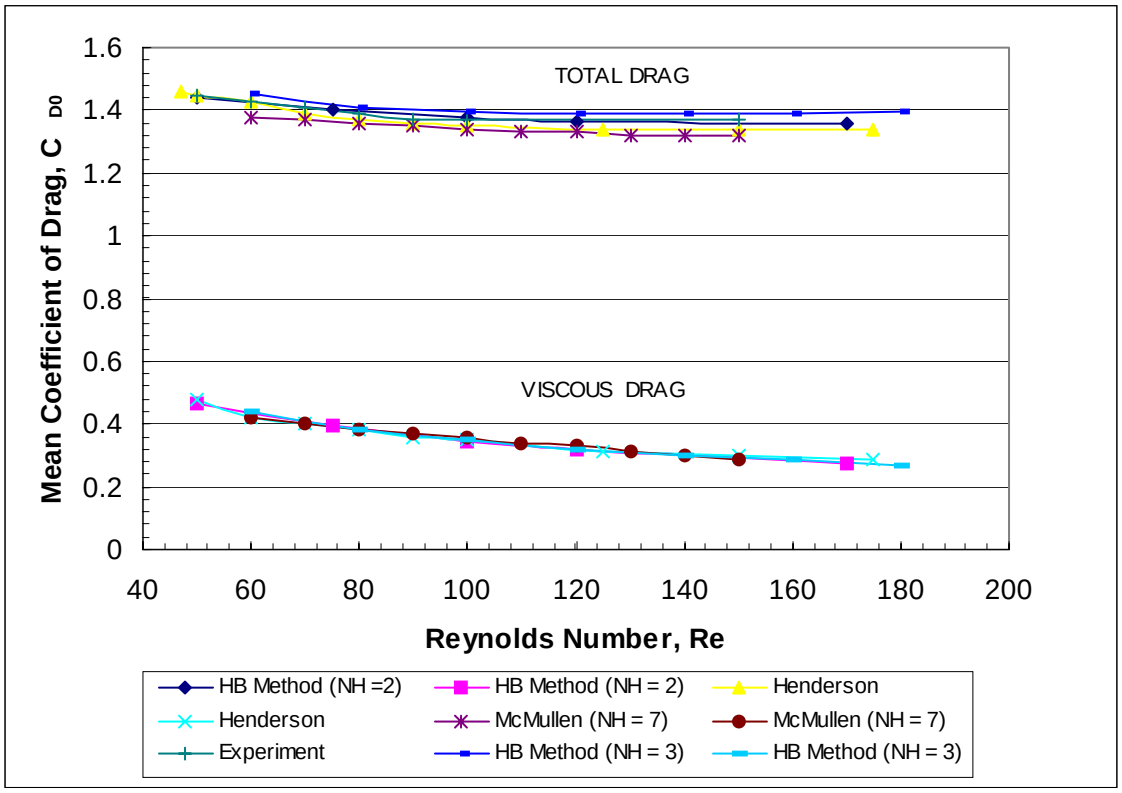

Figure 12. Comparison of Mean Coefficient of Drag versus Reynolds Number Data with Henderson and McMullen for Laminar Vortex Shedding

3.2 CYLINDER WITH PRESCRIBED MOTION

Next, the cylinder is forced to oscillate at a specified amplitude and frequency. In this case, there is a range of frequencies over which the shedding frequency will "lock-in" to the frequency of the vibrating cylinder. This synchronization effect was first observed by Bishop and Hassan and later measured by Koopman at low Reynolds numbers (Koopman 1967, 508). Cylinder vibration with frequencies near the shedding frequency can influence both the pattern and the phasing of vortices. Outside of this

region, the cylinder will oscillate at a frequency close to that of the stationary shedding frequency. Forced oscillations were achieved experimentally by using a shaking mechanism to generate a controlled motion at a range of amplitudes and Strouhal frequencies. Therefore, as the driving frequency is increased, two distinct behaviors are observed, inside and outside of the so-called lock-in regime.

Technique Used to Determine Bounds of Lock-In Region

To investigate this phenomenon numerically, the same HB solution methodology was used but with the cylinder vibrating in the transverse direction at a prescribed frequency. Koopman experimentally determined the lock-in region for Reynolds numbers of 100 and 200. In a first attempt to replicate the data, the code was run at a Reynolds number of 150 with a fixed amplitude for many different Strouhal numbers, and the solution residual was noted for each case. The solution residual within the lock-in region will converge to machine zero. Outside of this region, two distinct frequencies are observed experimentally; however the current HB method can only handle one frequency. Thus in the region where two frequencies are expected to be present, the current numerical method fails to converge. Extension of the HB method to treat two or more frequencies is possible and is the subject of current research. Figure 13 shows this behavior for two different Strouhal numbers, one inside and one outside of the synchronization region.

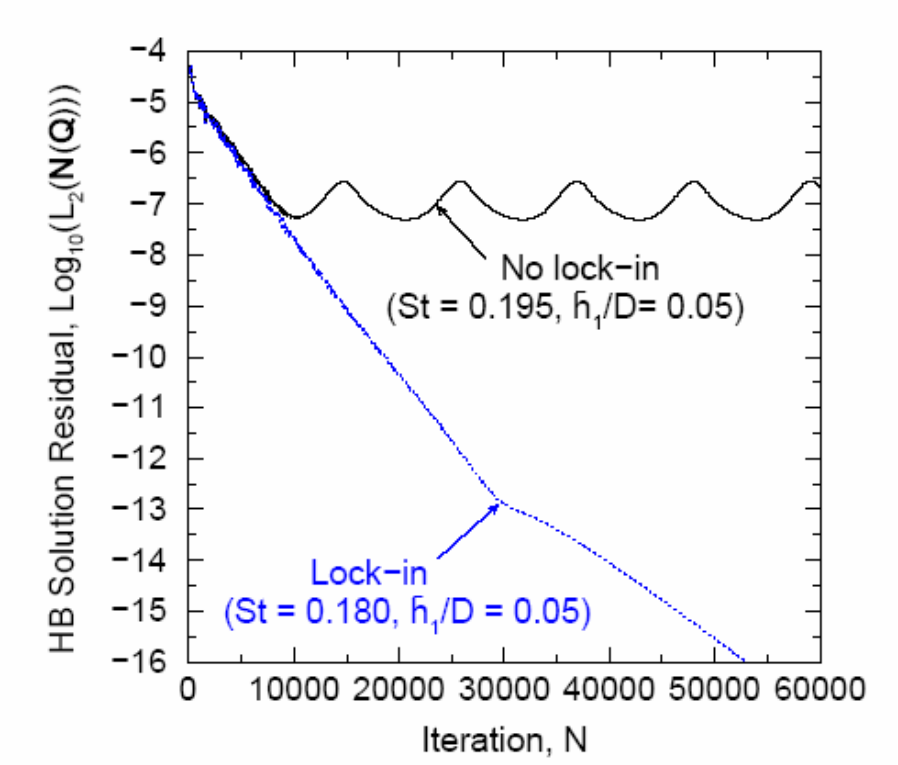

Figure 13. Behavior of Solution Residual In and Out of the Lock-in Region

Therefore, by repeating this procedure for various amplitudes, it was possible to establish an estimate of the left and right bounds on the lock-in region based on the HB solution behavior. However, it is difficult to determine the exact left and right bounds of the lock-in region due to the inability of the HB method to accurately determine the frequencies outside of the lock-in region where the cylinder is shedding at a different frequency than it is vibrating. Therefore, there is some subjectivity in assessing what constitutes a fully converged solution within the lock-in region.

Initially, a mesh size of 129x65 was used with a mesh boundary radius of forty diameters measured from the cylinder's center. A comparison between Blevins' data and the results obtained by the HB method is shown in Figure 14. The dimensionless amplitude is plotted versus the ratio of the frequency of the vibrating cylinder to the stationary shedding frequency. From the plot, it can be seen that there is good agreement

up to an oscillation amplitude of 0.05. However, above this amplitude, the HB solution begins to deviate greatly from the experimental values. This discrepancy may be due to the use of a coarse mesh, a large mesh boundary, or the code's limitation of the use of only 3 harmonics. As a result, a number of changes were made to achieve better agreement with Blevins' experimental data.

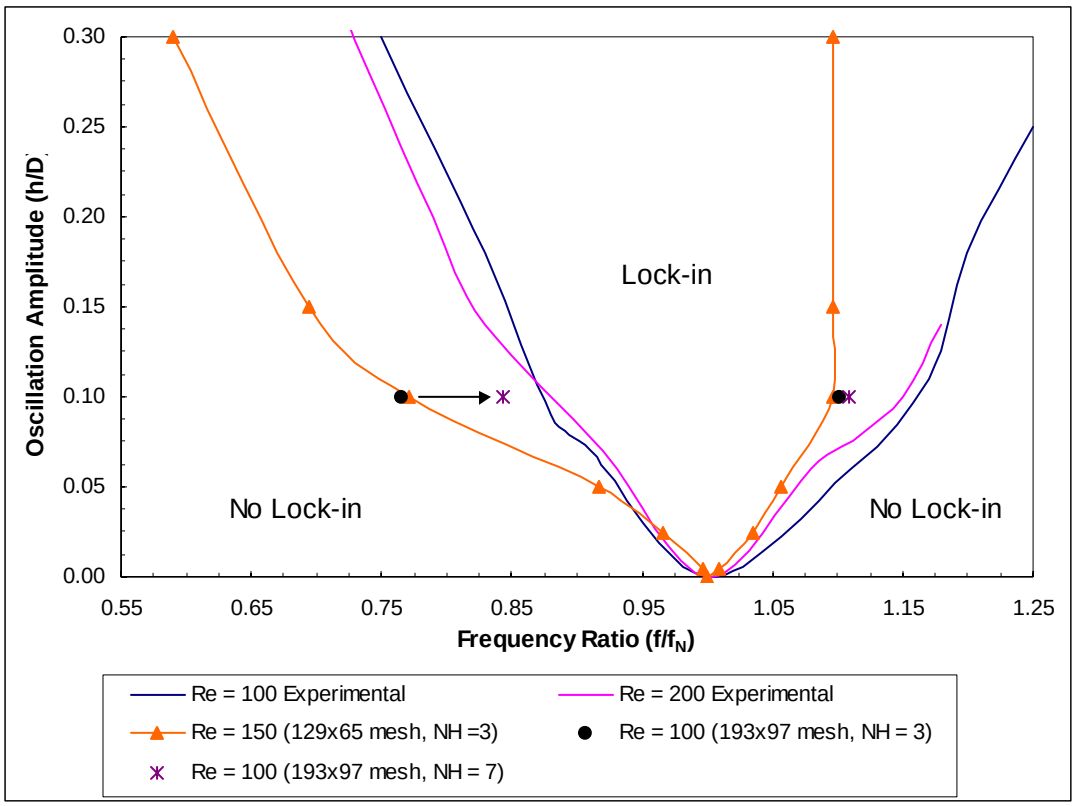

Figure 14. Demonstration of Lock-in Phenomenon

Effect of Mesh Refinement

The initial improvements involved utilization of finer meshes and a smaller mesh boundary. Both a 193x97 and a 257x129 mesh were considered as well as a mesh boundary of 20 times the diameter of the cylinder (20D) instead of 40D. Table 1 shows the results obtained from the mesh refinement study for dimensionless amplitude of 0.10. As can be seen, the use of a finer mesh improves the results at an amplitude of 0.10 but

there is still a significant difference in the bounds. Therefore, a further refinement is required to achieve better accuracy at higher vibratory amplitudes.

Addition of Filter to Reduce Far Field Boundary Effects

Due to the constraints of using the HB method with a large grid domain, the previous code limited the user to only three harmonics. In an attempt to avoid this problem, a subroutine was added to act as a filter for the HB method. The filter was designed to zero out the higher harmonics as you go farther and farther out in the domain, away from the cylinder where the wake effects are small. Therefore, it is possible to use as many as seven harmonics to achieve a more accurate solution. By examining Table 1, the results show that adding up to seven harmonics greatly improves the estimate of the left bound of the lock-in region and showed a slight improvement in the right bound. In addition, the results from the 193x97 mesh were added to Figure 20 to demonstrate the new bounds. Therefore, the filter was a valuable tool because it gave a way to study the effect of adding more harmonics to the solution. It was found that the use of more harmonics resulted in a better approximation to the experimental values obtained by Blevins. However, mesh size had only a small effect on the bounds of the lock-in region.

					Left Bound	Right Bound
Mesh Size	**Re**	**h/D**	**Radius**	**NH**	**f/f_N**	**f/f_N**
129x65	100	0.10	20	3	0.7656	1.1016
193x97	100	0.10	20	3	0.7656	1.1016
257x129	100	0.10	20	3	0.7891	1.1094
193x97	100	0.10	20	7	0.8438	1.1094
Experimental	100	0.10	-	-	0.875	1.1284
129x65	150	0.10	40	3	0.7708	1.0972

Table 1. Effect of Mesh and Harmonic Refinement on Modeling Blevin's Experimental Lock-in Region for Re = 100

Unsteady Lift for Prescribed Motion

In addition to determining the lock-in region, the unsteady lift was calculated. Tanida, et al. experimentally measured this quantity in a towing tank with 30 mm diameter test cylinders in which the lift and drag forces are sensed by strain gauges (Tanida 1973, 773). Oil was used as the fluid because it allows the unsteady aerodynamic forces on the oscillating cylinder to be measured with reasonable accuracy (Tanida 1973, 771). The study was conducted at a Reynolds number of 80 and a non-dimensional amplitude of 0.14. Once again, the HB method was used at these conditions and compared with the experimental data. A plot of the results can be found in Figure 16. The HB method shows remarkable agreement with the experimental results of Tanida, et al. The stability of the cylinder oscillation is dependent on the component of the unsteady lift force that is in phase with the oscillating velocity (Tanida 1973, 774). Therefore, the cylinder will be unstable if the imaginary part of the unsteady lift coefficient is greater than zero, which is characteristic of negative aerodynamic damping.

Real and Imaginary Part of the Unsteady Lift

The real and imaginary components of the lift coefficient are plotted below. The plot of the imaginary component shows the system is stable for St = 0.1000 to St = 0.1300 and then becomes unstable throughout the rest of the lock-in region. The stability of the system is determined by assuming harmonic motion in which

$$C_L = | C_L | e^{-i\omega t} = | C_L | e^{-\omega_R t} e^{\omega_I t} \tag{33}$$

where a negative value indicates a stable solution and a positive value gives an exponentially growing term which causes instability. A sensitivity study was conducted to determine the effect of including more and more harmonics. There does not appear to

be a substantial benefit to keeping more than two harmonics in the HB solution for the parameter range studied here.

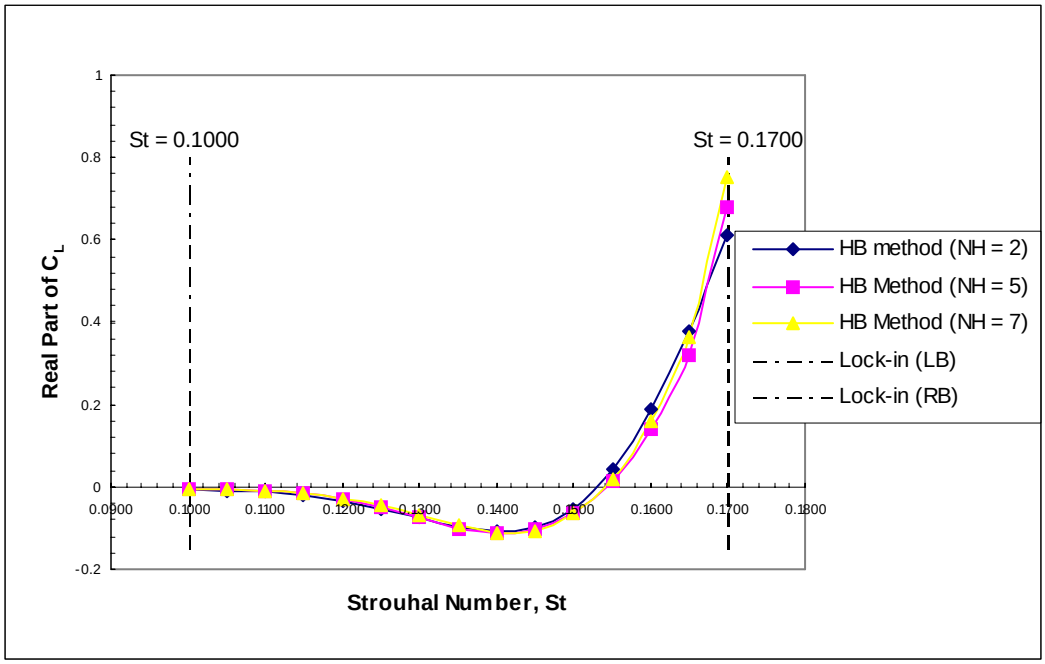

Figure 15. Magnitude of the Real Part of the Unsteady Lift Coefficient versus Strouhal Number for a Single Cylinder Oscillating Transversely (h/D = 0.14)

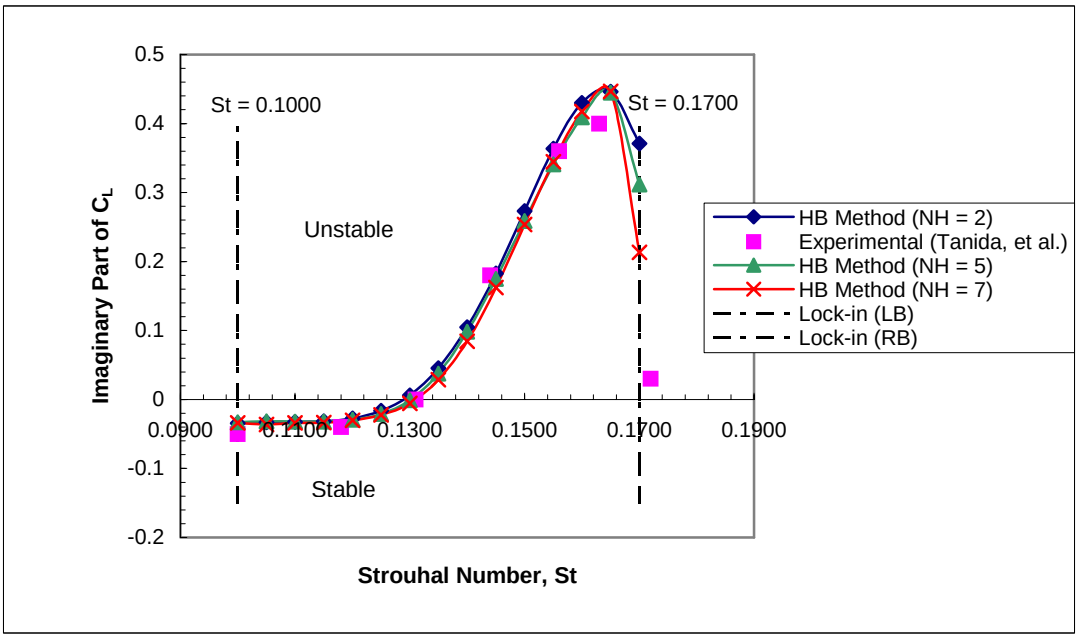

Figure 16. Magnitude of the Imaginary Part of the Unsteady Lift Coefficient versus Strouhal Number for a Single Cylinder Oscillating Transversely (h/D = 0.14)

Amplitude of the Unsteady Lift

In addition, a plot of the amplitude of the unsteady lift coefficient was constructed. By examining the plot in Figure 17, the amplitude appears to steadily increase throughout the lock-in region until a peak displacement is reached. When compared to the stationary cylinder case, nearly the same C_L value is obtained for Re = 80. In addition, the cylinder was also forced to oscillate at half the vibratory amplitude, i.e. h/D = 0.07 and it was discovered that lock-in region became smaller but the amplitude of the lift coefficient fell on the same curve as the h=0.14 case. The cylinder was also forced to vibrate at higher amplitudes and the lift coefficient actually decreased (see Figure 18). Therefore, cylinder motion does not dramatically affect the lift coefficient for oscillation amplitudes up to about h/D = 0.40. Therefore, the lift coefficient appears to be relatively independent of the prescribed amplitude when the cylinder is driven at an amplitude of approximately 10 percent or less of the cylinder's diameter and for higher vibratory amplitudes, the lift coefficient decreases. This has important implications for the study of non-synchronous vibrations of turbomachinery blades because it may not be necessary to couple the NSV fluid dynamic solution with blade motion for sufficiently small blade amplitudes, which is a much easier computation.

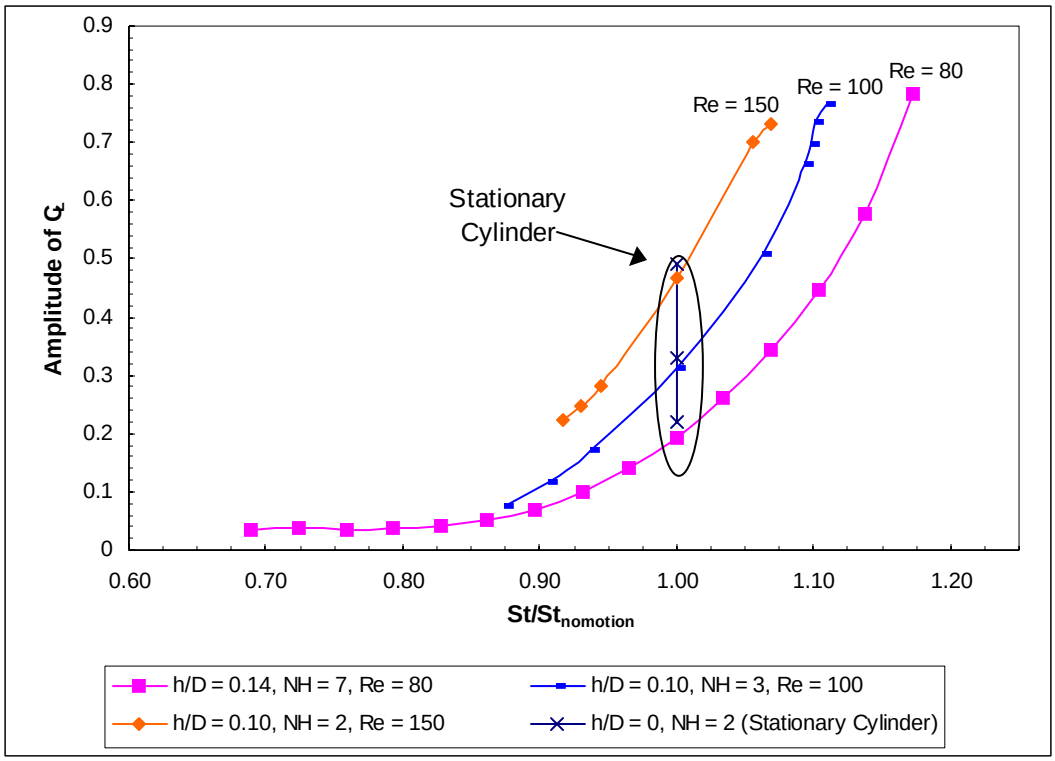

Figure 17. Amplitude of the Unsteady Lift versus Strouhal Number for a Reynolds Number of 80 and a Mesh Size of 129x65 with a Radius of 20

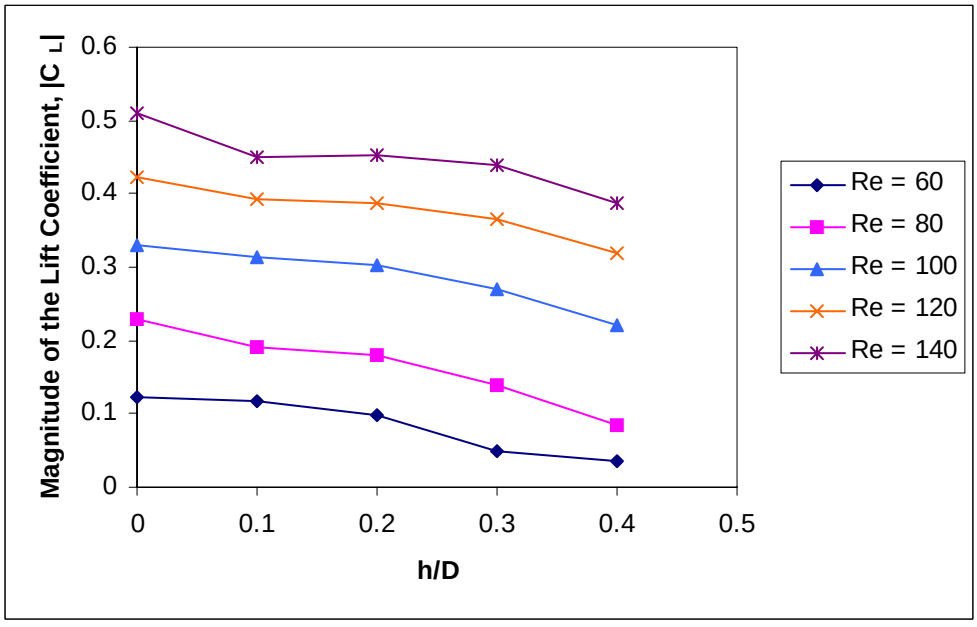

Figure 18. Effect of Oscillation Amplitude on the Magnitude of the Unsteady Lift Coefficient, $|C_L|$

Phase Shift as a Function of Strouhal Number

Another important characteristic of the lock-in region is the phase angle as a function of the Strouhal number within the lock-in region. The phase angle is a measure of the phase difference between the displacement of the cylinder and the lift force. By examining Figure 18 below, the cylinder lift undergoes an abrupt 180 degrees phase shift between the shedding and the cylinder motion at about a Strouhal number of 0.1500. For a Reynolds number of about 80, the stationary cylinder shedding frequency was found to be about St = 0.1450 using the HB method. Therefore, it appears that this 180 degrees phase shift occurs as the cylinder vibration frequency passes through the natural shedding frequency. This could be explained by Zdravkovich's physical observation of the flow behind the cylinder. By examining the flow over an oscillating cylinder, it is noted that the vortices tend to shed when the cylinder is near its maximum displacement (Blevins 1990, 56). Zdravkovich found that for frequencies below the natural shedding frequency, the vortex is shed from the side opposite that experiencing its maximum displacement. However, for frequencies above the shedding frequency, the vortex is shed from the same side as the max displacement (Sarpkaya 2003, 64). Therefore, the phase shift may be due in part to a switch in the timing of the shedding of the vortices. The stability of the system is consistent with the plot of the imaginary coefficient of lift. A phase shift of zero degrees refers to the condition in which the force and displacement are in-phase and no work is being done.

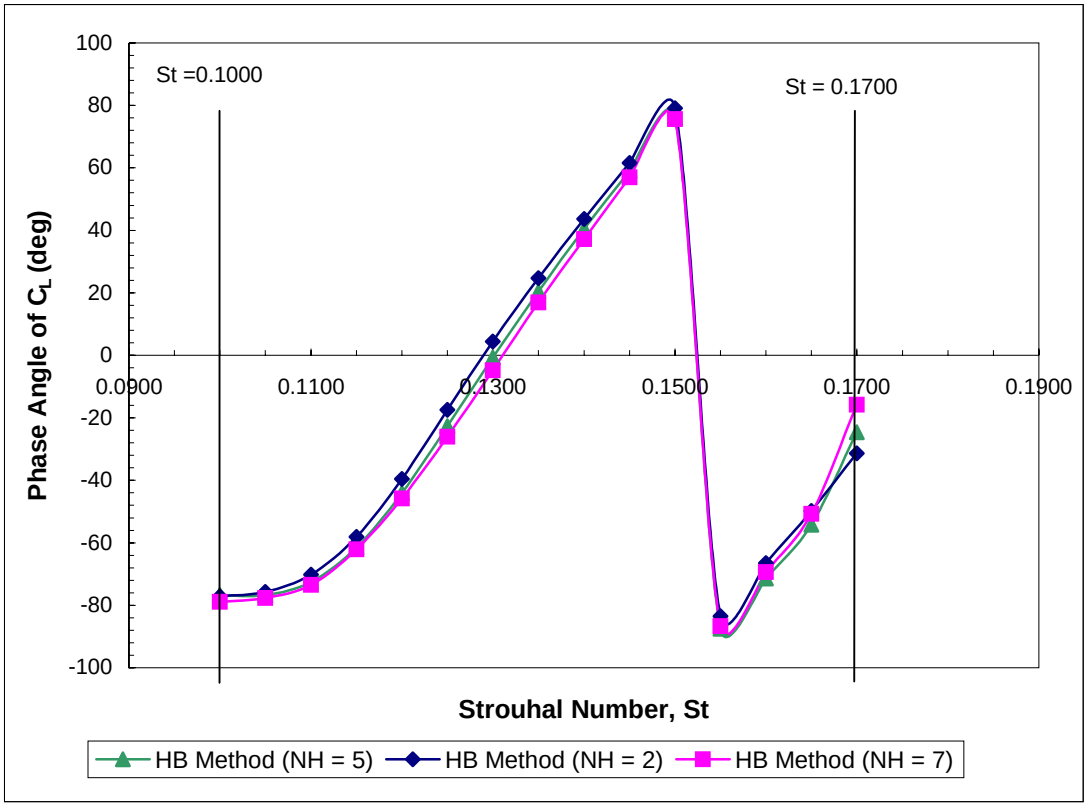

Figure 19. Phase Angle Between the Lift and Displacement Within the Lock-In Region

Aerodynamic Damping

In addition, the aerodynamic damping was also calculated. Aerodynamic damping is a result of fluid forces acting on the structure. As can be seen from Figure 19, the damping becomes increasingly negative until it reaches a minimum value and then starts to increase again. A negative aerodynamic damping results in a net energy input to the cylinder vibration. The most unstable damping coefficient occurs at a Strouhal number of 0.1600 which coincides with the point for which maximum work is being done.

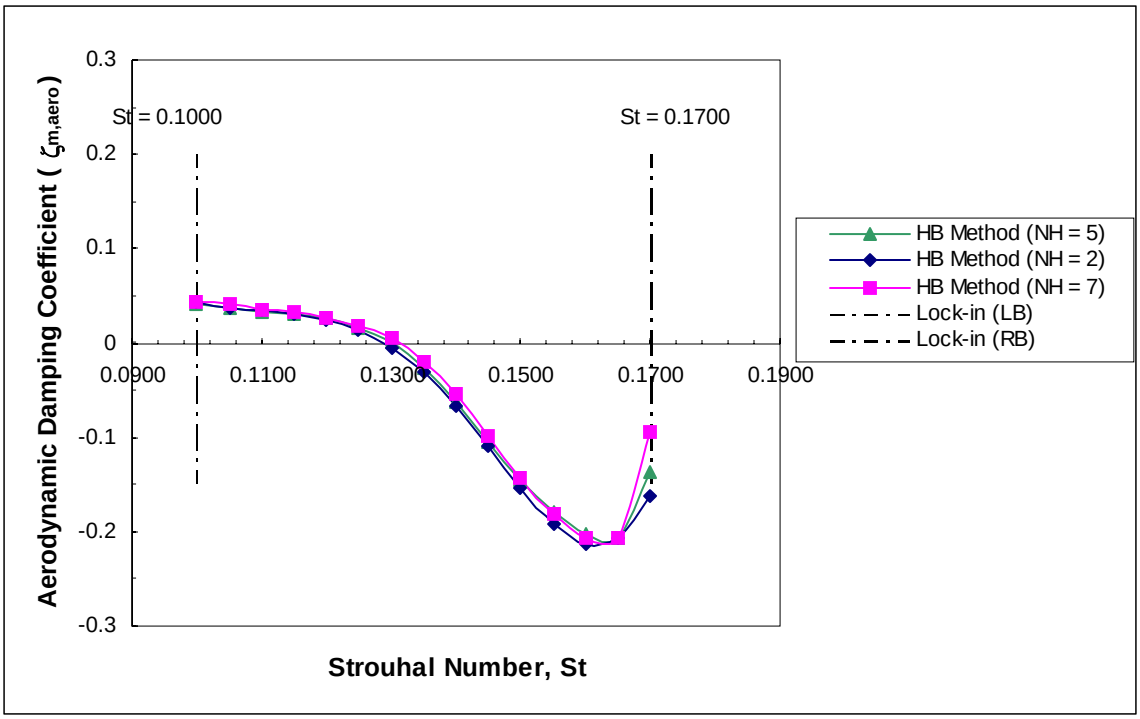

Figure 20. Aerodynamic Damping in the Lock-in Region as a Function of Strouhal Number

Therefore, by examining the amplitude, phase angle, and damping coefficient within the lock-in region, various flow characteristics were deduced. Specifically, the stability of the flow, the frequency for which the maximum response occurs, and the behavior at the endpoints of the lock-in region were found and compared with the physics of the flow behind a cylinder.

Mean Cylinder Drag for Prescribed Motion

In addition to the fluctuating lift forces on the cylinder, the mean drag was also calculated as a function of Strouhal number. Figure 20 shows the results obtained by the HB method as compared to the experimental results of Tanida. By examining the plot, it can be seen that the drag coefficient steadily increases within the lock-in region until it reaches a maximum around $C_{D0} = 1.63$ at St = 0.1650 for the HB method. On the other hand, Tanida's results indicate a maximum value of $C_{D0} = 1.87$ at St = 0.1500. However,

despite this discrepancy, the overall trend appears to be the same and the HB method shows relatively good agreement with Tanida's experimental data. Therefore, the HB method is also capable of determining the drag forces on a cylinder when it is subjected to a prescribed motion.

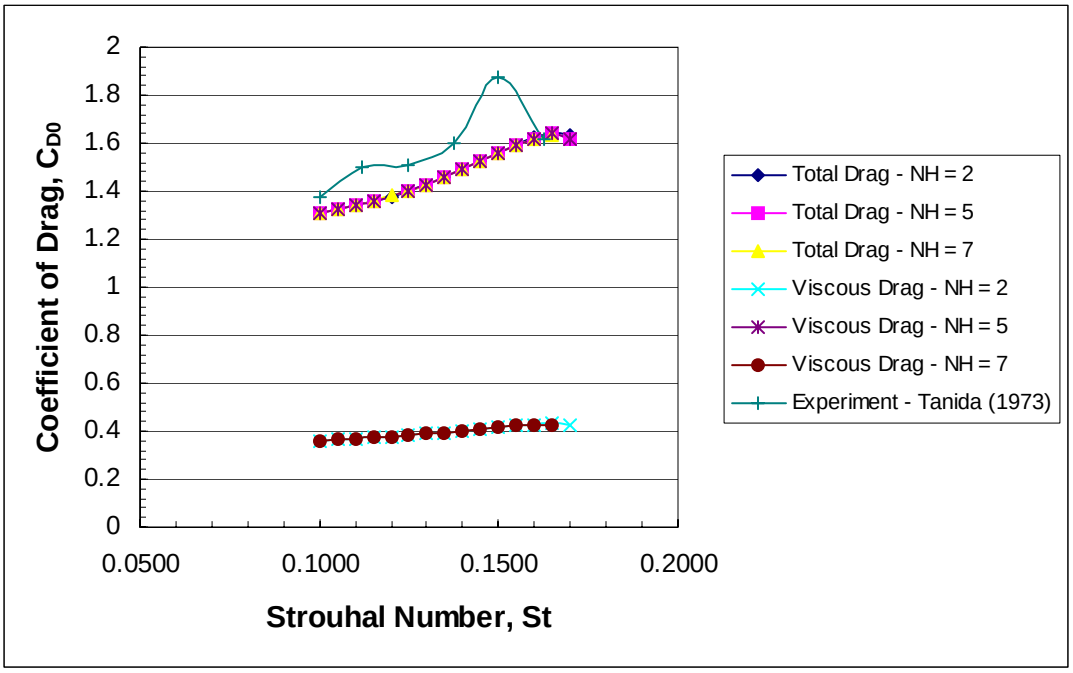

Figure 21. Comparison of the Mean Coefficient of Drag versus Strouhal Number Within the Lock-in Region

3.3 ELASTICALLY MOUNTED CYLINDER

Finally, it is important to determine the response characteristics of a vortex-excited spring supported cylinder in the stable, laminar flow regime. In this case, as the flow velocity is increased or decreased, the shedding frequency can approach the natural frequency of the structure. At a critical velocity, the shedding frequency will lock-in to the structure frequency (Blevins 1973, 21). In the synchronization region, resonant oscillation conditions can occur and produce large amplitude responses. Therefore, by determining the interaction between the flow oscillations and the cylinder motion, it will

be possible to predict the cylinder oscillation frequency and the resultant cylinder amplitude.

Aeroelastic Cylinder Model

This cylinder aeroelastic "lock-in" problem is modeled by a single degree of freedom spring-mass-damper system excited by a transverse lift force expressed as L′, the lift per unit span. A schematic of this system can be seen in Figure 22. As can be seen, the cylinder is mounted on a linear spring of stiffness of k and a structural damping coefficient of d. The external force on the cylinder is represented by the unsteady lift generated by the trailing vortices. The governing equation that describes this system is:

$$m\frac{d^2h}{dt^2} + d\frac{dh}{dt} + kh = \frac{1}{2}\rho_\infty U_\infty DsC_{L'} \tag{34}$$

where m is the mass of the cylinder, d is the damping coefficient, k is the cylinder spring stiffness, ρ_∞ is the fluid density, U_∞ is the fluid velocity, D is the cylinder diameter, s is the cylinder span, $C_{L'}$ is the cylinder lift coefficient, and h is the transverse displacement of the cylinder.

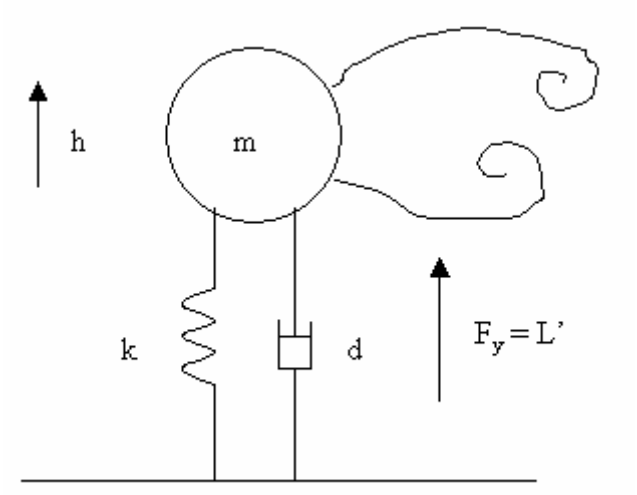

Figure 22. One-Degree-of-Freedom Model of a Vortex-Excited Cylinder

Next, one can assume simple harmonic motion so h and $C_{L'}$ can be represented as

$$h = h_1 e^{j\omega t},\ C_{L'} = C_{L_1} e^{j\omega t} \tag{35}$$

As a result of this substitution, equation (38) becomes:

$$(-\omega^2 m + j\omega d + k)h_1 - \frac{1}{2}\rho_\infty U_\infty{}^2 DsC_{L'} = 0 \tag{36}$$

Non-Dimensional Parameters

In practice, it is more common to study the non-dimensionalized form of this equation because it reduces the number of parameters and also, makes it easier to compare with experimental results. As a result, some new dimensionless parameters should be introduced. The first parameter is the natural frequency of the system, which is independent of any initial excitations. It is expressed as

$$\omega_0 = \sqrt{\frac{k}{m}} \tag{37}$$

Another parameter of interest related to the natural frequency is the damping factor. This value characterizes the energy dissipated by the cylinder as it vibrates. It is described by the following equation:

$$\zeta = \frac{d}{2m\omega_0} \tag{38}$$

Another factor controlling the fluid-structure interaction is the mass ratio. It is the ratio of the mass of the cylinder to the mass of the fluid displaced by the cylinder. It provides a measure of the buoyancy effects and the inertia of the model as compared to the fluid (Blevins 1973, 7). It is given by:

$$\mu_m = \frac{4m}{\pi\rho_\infty D^2 s} \tag{39}$$

It is also common to define a non-dimensional vertical displacement coordinate. Therefore, the plunge coordinate can be divided by a characteristic length such as the diameter of the cylinder. The new coordinate is defined as:

$$h_1' = \frac{h_1}{D} \tag{40}$$

The final parameter represents a ratio of the fluid frequency to the structural frequency and is given by:

$$\mathrm{K} = \frac{2\pi\nu_\infty}{\omega_0 D^2} \tag{41}$$

Using all these dimensionless parameters, the governing equation can be greatly simplified. In general, the final equation can be written as:

$$(-\mathrm{K}^2\,\mathrm{Re}^2\,St^2 + 2j\mathrm{K}\,\mathrm{Re}\,St + 1)h_1' - \frac{\mathrm{K}^2\,\mathrm{Re}^2}{2\mu_m\pi^3} C_{L_1}(\mathrm{Re}, St) = 0 \tag{42}$$

By separating this equation into its real and imaginary parts, a system of two equations is produced. Thomas, et al. initially demonstrated this method in 2002 (Thomas, Dowell, and Hall 2002, 645). These equations can be solved simultaneously for the two unknowns, Reynolds number and Strouhal number, for a specified h_1'. The nominal residual of the real and imaginary parts can then be written in the following form:

$$R(L) = \begin{bmatrix} (-\mathrm{K}^2\,\mathrm{Re}^2\,St^2 + 1)h_1' - \dfrac{\mathrm{K}^2\,\mathrm{Re}^2}{2\mu\pi^3}\mathrm{Re}[C_{L_1}(\mathrm{Re}, St)] \\ (2\mathrm{K}\zeta\,\mathrm{Re}\,St)h_1' - \dfrac{\mathrm{K}^2\,\mathrm{Re}^2}{2\mu\pi^3}\mathrm{Im}[C_{L_1}(\mathrm{Re}, St)] \end{bmatrix} = 0 \tag{43}$$

where L is a vector of the unknown variables, Re and St.

Application of Newton-Raphson Technique

The Newton-Raphson technique is then used to solve for the correct combination of Reynolds number and Strouhal number for which the residual goes to zero. The Newton-Raphson technique is an efficient and stable way to quickly solve the system of equations (Thomas, Dowell, and Hall 2002, 645). The method requires the user to choose an initial value for Reynolds number and Strouhal number. The method then uses the HB solver to determine the real and imaginary parts of the unsteady lift coefficient. Next, the Reynolds number is perturbed by a small amount and the change in the forces with respect to Reynolds number is evaluated. The procedure is repeated for the Strouhal number. In vector notation, this procedure can be expressed as:

$$\left[\frac{\partial R(L)}{\partial L}\right] = \left[\frac{\partial R}{\partial \mathrm{Re}} \quad \frac{\partial R}{\partial St}\right] \tag{44}$$

where $\frac{\partial R}{\partial \mathrm{Re}}$ and $\frac{\partial R}{\partial St}$ are given by the following relations,

$$\frac{\partial R(L^n)}{\partial \mathrm{Re}} \approx \frac{R(L^n, \mathrm{Re}^n + \varepsilon) - R(L^n, \mathrm{Re}^n)}{\varepsilon} \tag{45}$$

$$\frac{\partial R(L^n)}{\partial St} \approx \frac{R(L^n, St^n + \varepsilon) - R(L^n, St^n)}{\varepsilon} \tag{46}$$

for small values of ε. The resulting values can be put into matrix form and then the inverse is taken. This quantity is then multiplied by the original solution and subtracted from the initial guess of the Strouhal number and Reynolds number. Therefore, this is an iterative process and can be written as:

$$L^{n+1} = L^n - \left[\frac{\partial R(L^n)}{\partial L}\right]^{-1} R(L^n) \tag{47}$$

This gives a new update for Re and St and the process is repeated until the solution converges. This technique is advantageous because it only requires a few iterations to achieve convergence.

Preliminary results by Jeffrey P. Thomas show that this is a viable method for predicting the Strouhal number and Reynolds number of the self-excited cylinder for a range of Reynolds numbers. A plot of these results is shown below in Figure 22.

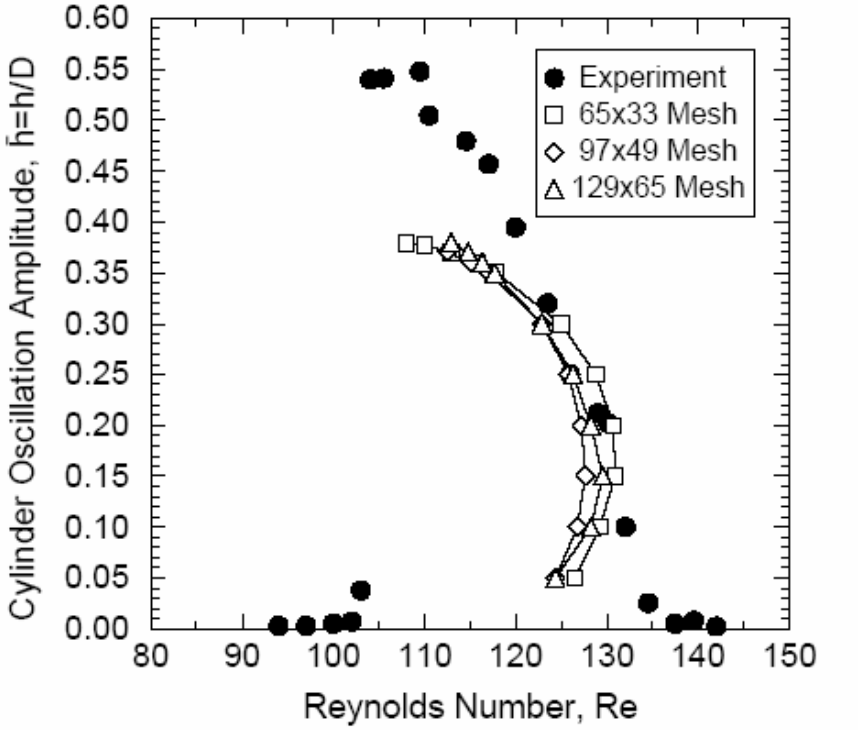

Figure 23. Cylinder Oscillation Amplitude versus Reynolds Number with Varying Mesh Sizes and Comparison with the Experimental Data (Thomas 2004)

An interesting feature of this figure is the fact that there are two different amplitudes obtained for one Reynolds number, which is not possible to obtain experimentally. This may be explained by the fact that two solutions are present – a stable and an unstable one. Therefore, the experiment will not capture the unstable solution and will jump directly to the stable one. In addition, a plot of the Strouhal number as a function of Reynolds

number was constructed for frequencies within the lock-in region. The results show that the HB method predicts the relationship between Reynolds number and Strouhal number fairly well within the lock-in region. Therefore, the HB method can be coupled with a Newton-Raphson solver to accurately model the aeroelastic cylinder case.

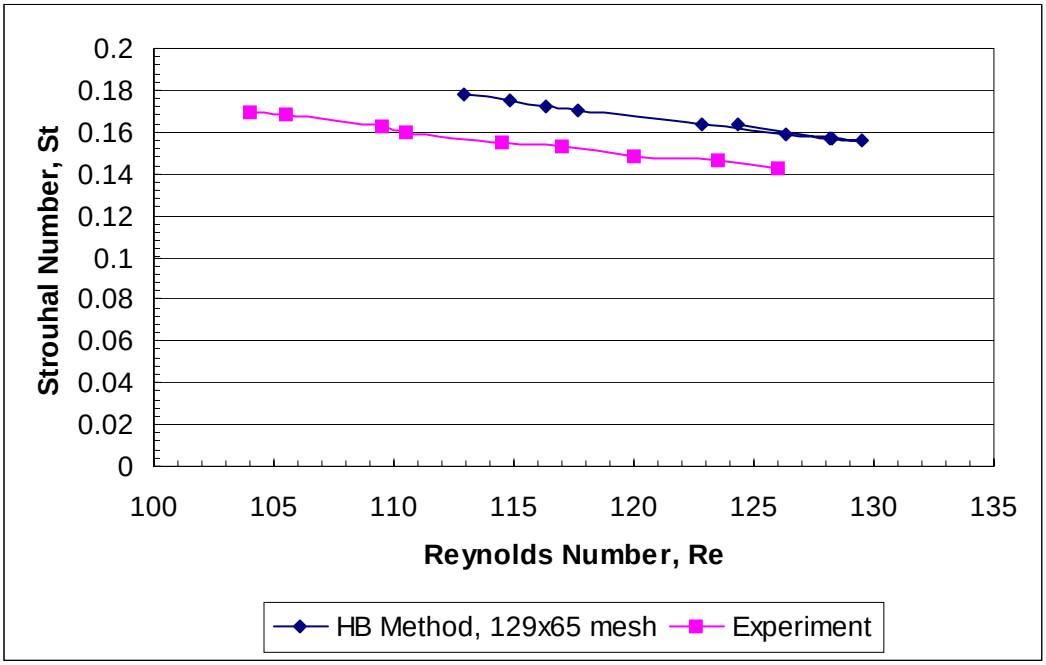

Figure 24. Comparison of Relationship Between Reynolds Number and Strouhal Number for Aeroelastic Case

Experimental Procedure and Results

To validate these results, the solution was compared with those obtained experimentally by Anagnostopoulos and Bearman. They conducted their experiment in a water channel by mounting a 1.6 mm diameter circular cylinder on two steel springs on a horizontal shaft (Anagnostopoulos and Bearman 1992, 41). Using the experimental parameter values given for the natural frequency, the damping factor and the mass ratio and calculating K from given measurements, a direct comparison can be made. Anagnostopoulos and Bearman examined Reynolds numbers in and out of the lock-in region. As predicted, they found that at a Reynolds number before lock-in, the vortices

were shed at the Strouhal frequency but the cylinder was oscillating at a different frequency so two frequencies were present in the system (Anagnostopoulos and Bearman 1992, 43). However, when the Re was increased to 104, the cylinder oscillation frequency synchronized with the shedding frequency and the amplitude of the cylinder oscillations greatly increased. They found that the maximum oscillation amplitude occurred near the middle of the lock-in region (Anagnostopoulos and Bearman 1992, 47). When the Reynolds number was increased further to a value of about 126, the shedding becomes unlocked once again. Therefore, by integrating the Newton-Raphson technique into the HB solver, a solution for the cylinder self-excited aeroelastic problem has been obtained and compared with Anagnostopoulos' experimental data.

3.4 TWO-DIMENSIONAL AIRFOIL (C1 CASE)

Having verified that the technique can accurately predict the shedding frequency for flow about a cylinder, we next considered a flow instability about a two-dimensional airfoil section of a modern compressor blade (C1) operated at an off-design condition. First, a time domain version of the flow solver was generated and the unsteady normal force on the blade was determined as a function of time (see Figure 25). It is noted that the amplitude has converged at 50 time steps / iteration. This was then FFT'ed to determine the frequency content with the results shown in Figure 25 (right side).

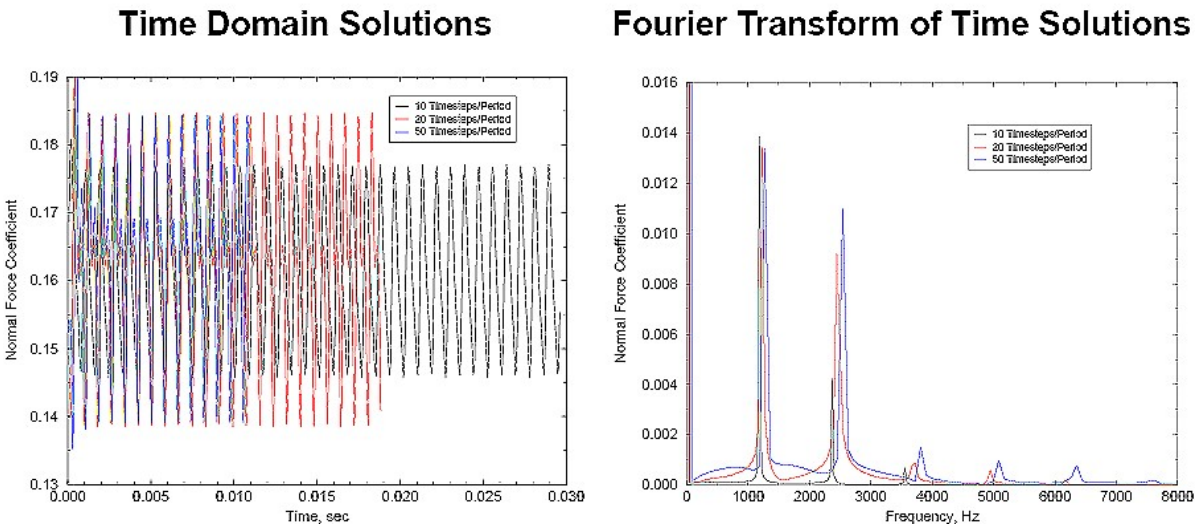

Figure 25. Time Domain Solution and Fourier Transform of Time Solutions for Three Different Timesteps/Period (IBPA = 0)

To verify this frequency, the results were then compared with those obtained using the HB method. The blade geometry as well as the Mach contours for the steady case is shown in Figure 26. First, a "steady" flow solution was obtained. Figure 27 shows that the solution residual does not approach zero. Instead, the residual oscillates. This oscillation is an indication of an underlying physical flow instability. However, because the steady flow solver uses local time stepping and multi-grid acceleration, we cannot infer the frequency of the physical instability from this calculation.

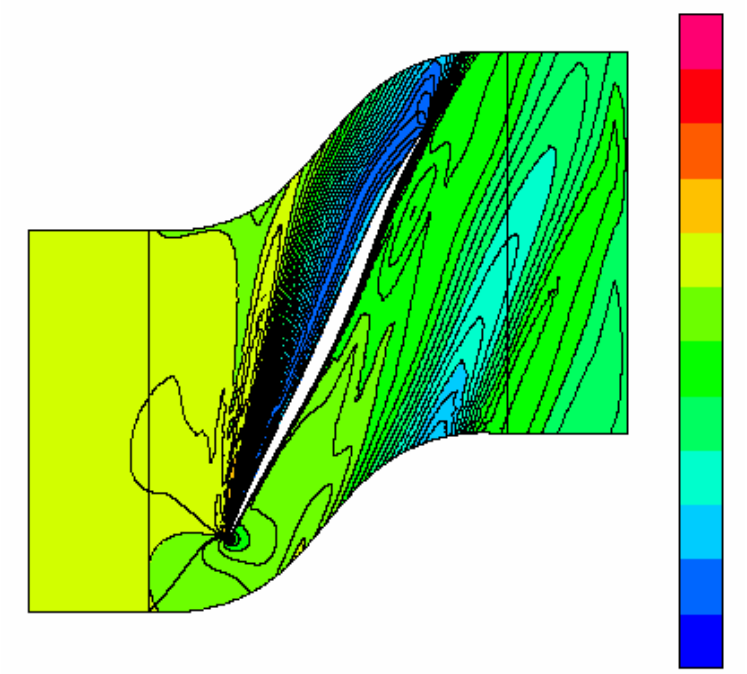

Figure 26. Mach contours for the Steady Solver for 2-D Flow About C1 Compressor Blade

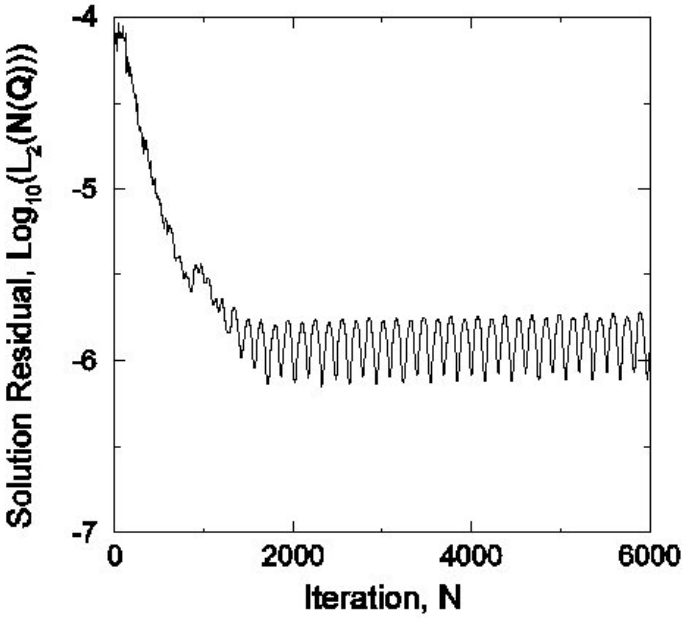

Figure 27. Convergence History of Steady Flow Computation for 2-D Flow About C1 Compressor Blade

Next, the nonlinear harmonic balance solver was used to compute the physical frequency with interblade phase angle of zero degrees. The procedure is to search for the

frequency that allows the harmonic balance flow solver to converge to a zero residual. Figure 28 shows the solution residual of the harmonic balance solver as a function of frequency for the zero interblade phase angle case. Note that a frequency of about 1250 Hz, the residual (for five harmonics) drops dramatically to zero, indicating that this is the frequency of the flow instability. Note the very narrow trough in the residual curve in Figure 28, complicating the search for the correct frequency. An alternative procedure is to search for the frequency that produces a constant phase in a global quantity such as the first harmonic of the lift using the same method as described above for the cylinder. Figure 29 (left side) shows the phase change per iteration of the harmonic balance flow solver when the convergence reaches a steady state. In this case, the phase change is nearly linear with frequency. This makes interpolation to the correct frequency a simple matter, and requires many fewer calculations.

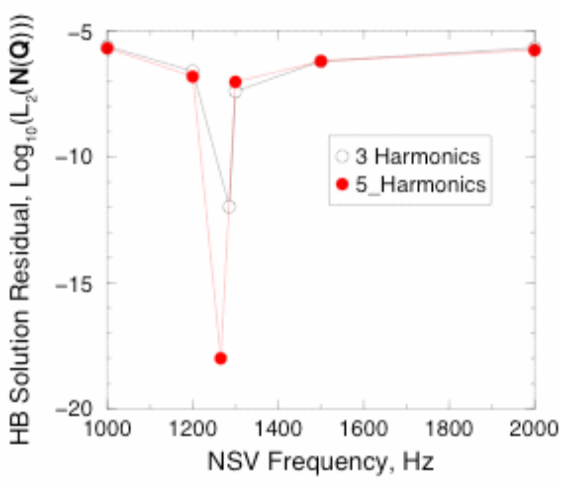

Figure 28. Residual of Harmonic Balance Solver (2D C1 Blade, IBPA = 0)

As can be seen in Figure 29, there is excellent agreement between the FFT'ed time domain results and the HB method frequencies. However, it appears that the HB method over predicts the amplitude of the first harmonic force coefficient and under

predicts the second harmonic. The higher harmonic amplitudes show good agreement. Therefore, the HB method is a very effective tool for determining the NSV frequency but does not accurately predict the amplitude for the first and second harmonics for this 2-D test case.

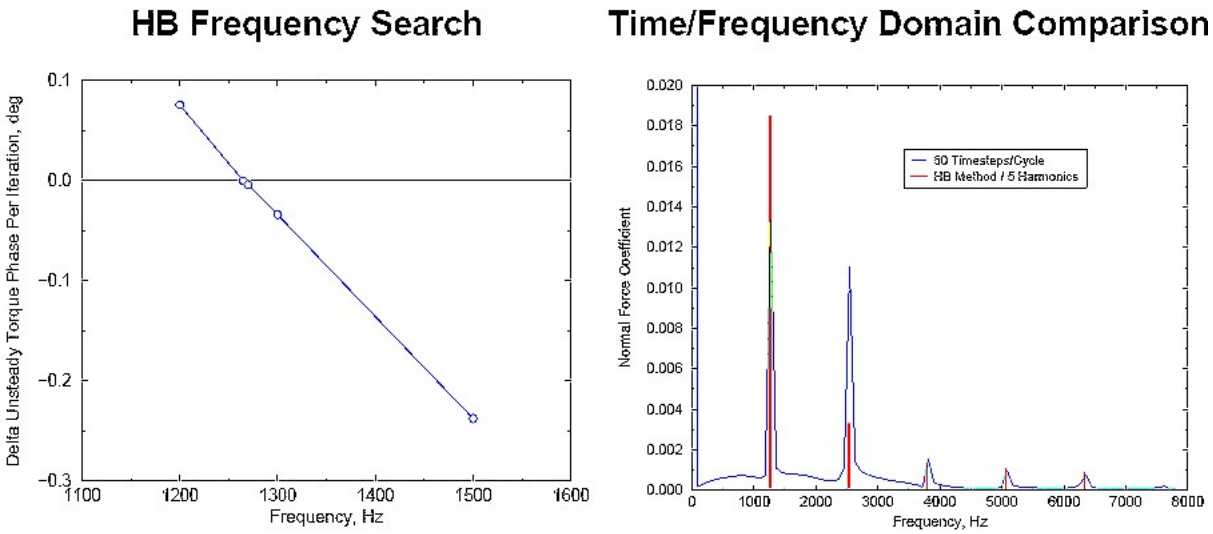

Figure 29. 2D C1 Case: HB Frequency Comparison with Time Domain Solution (IBPA = 0)

3.5 THREE-DIMENSIONAL CASES

Next, the HB methodology was applied to three-dimensional real world turbomachinery blade applications. Based on input from industry, NSV was encountered in experimental rig testing for two of the three test cases. In particular, the study examined a modern first stage compressor rotor blade (C1), a modern first stage fan blade (H1), and a modern fan vane blade (H2). Although NSV was not encountered for the H1 case, an analysis was performed to show that NSV is not predicted.

C1 CASE

The first case studied was a compressor rig test where the first stage modern compressor blades encountered NSV. For this test, there were 35 rotor blades and 56

inlet guide vanes (IGV's). Complete details of the study can be found in Kielb's paper entitled, "Blade Excitation by Aerodynamic Instabilities – A Compressor Blade Study" and are summarized below. The stage 1 blades are observed to experience a significant first torsion mode (1T) response at lower speed that shifts to a second torsion mode (2T) response at somewhat higher speed. Figure 30 shows a typical plot of blade response frequency and amplitude versus rotational speed. The vertical lines at fixed values of rotor speed and frequency are a measure of blade response amplitude at that frequency. The response at low speed is moderate separated flow vibration (SFV) response of the first flex (1F) and 1T modes. SFV is a broadband buffeting response of the blades. This SFV 1F response is followed at higher speeds by a significant NSV, which excites the 1T mode to a high level of response. This response switches from a higher frequency (2661 Hz) excitation to a lower frequency (2600 Hz) excitation at a somewhat higher speed. As the speed increases, the response switches to a 2T mode excitation. The NSV excitation of the 1T mode exists from approximately 12700 to 12880 rpm.

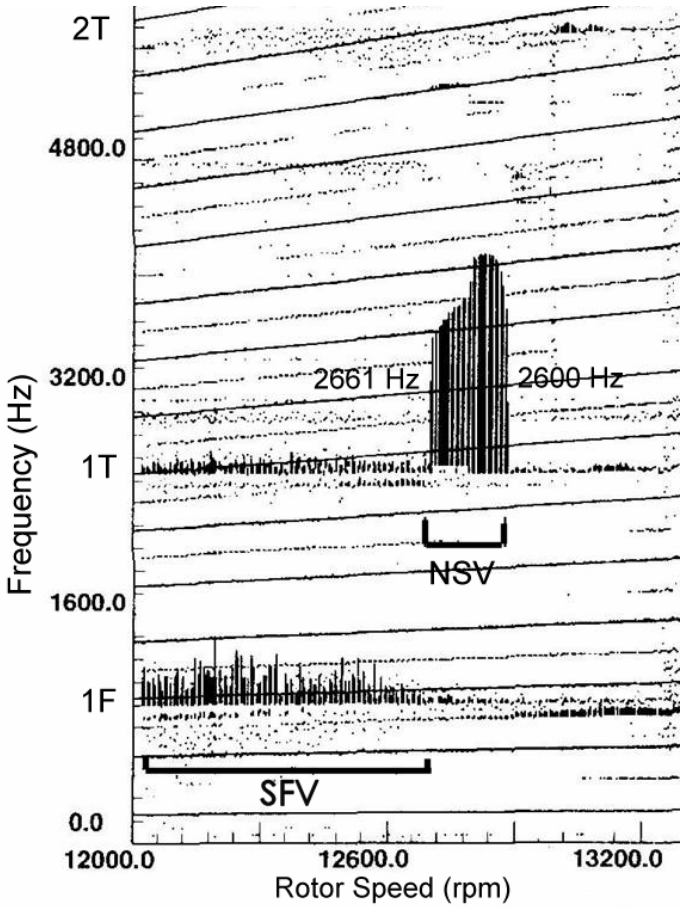

Figure 30. Strain Gage Response of First-Stage Rotor Blades of Compressor Rig

Unsteady pressure was also measured on the compressor casing at numerous axial and circumferential locations. Example data from a pressure transducer (located aft of the rotor 1 blades near the stage 1 vanes) is shown in Figure 31. Significant response at frequencies of 3516 Hz and 3662 Hz was observed at all axial and circumferential measurement locations.

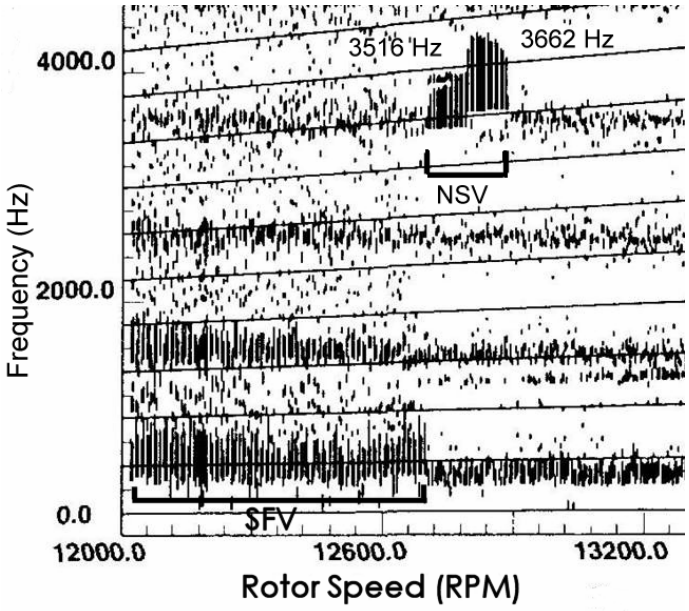

Figure 31. Casing Unsteady Pressure Measurements

First, the unsteady CFD code, TURBO, (Chen & Briley (2001)), was used to investigate the NSV observed in the rig test. A single row, five passage, mesh modeled one-seventh of the rotor circumference. The mesh, consisting of 188 axial, 56 radial, and 280 circumferential grid points, contained approximately three million grid points. Using TURBO, the analysis took about six months to run on a single processor. The local unsteady static pressures from the periodic CFD solution were investigated at many locations on the blade surface near the blade tip. This is shown in Figure 32, where the unsteady static pressures in passage three, near the leading edge on the pressure side, are presented. As can be seen, the unsteady pressure content at 2365 Hz and 4370 Hz is much greater than that at the vane passing frequency. The predicted NSV frequency (2365 Hz) is approximately 9% lower than that measured in the rig test. The TURBO results show that NSV are primarily a coupled, suction side vortex unsteadiness (near 75% span) and tip flow instability.

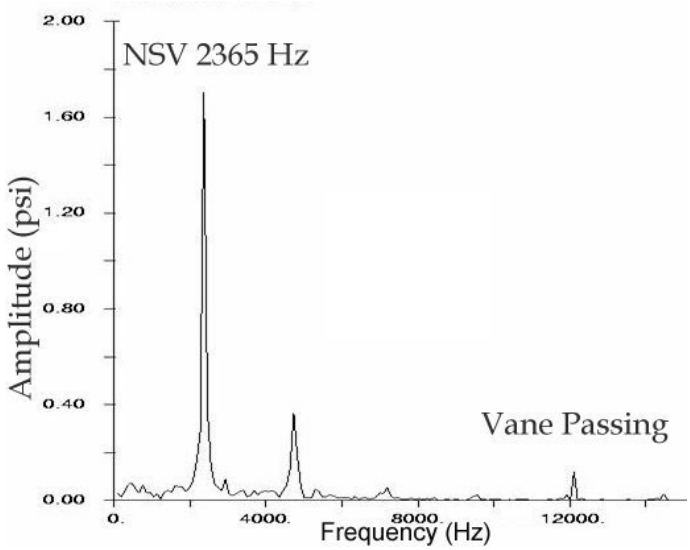

Figure 32. Unsteady Static Pressure Near Tip Pressure Side Near Leading Edge

In an attempt to replicate these results, similar conditions were used and the analysis was performed using Duke University's time domain and HB computational methods. The blade was excited at approximately 2.6 Khz. A time domain CFD analyses was conducted using the running clearance of 0.020 in., zero interblade phase angle, and $p_{exit}/p_{exitCAFD} = 1.000$ where CAFD is the exit pressure for which NSV was encountered in the experiment. An NSV frequency of 2.9 Khz was predicted (see Figure 33). We next used our harmonic balance method on this case. HB solution stability problems were encountered when running at the NSV speed. The phase change per iteration of the unsteady torque is shown in Figure 34 for five assumed frequencies with the same conditions as the time domain case. As can be seen the phase change reaches a constant value for 2.5 and 2.6 KHz. For 2.6 and 2.75 KHz the phase change does not converge to a constant value. This is likely because the fluid dynamic instability contains multiple (irrational) frequencies.

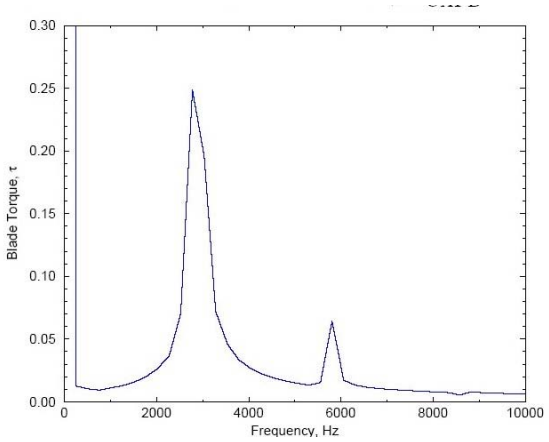

Figure 33. 3D C1 Case: FFT of Time Domain Solution (IBPA = 0, running clearance, $p_{exit}/p_{exitCAFD}$ = 1.000)

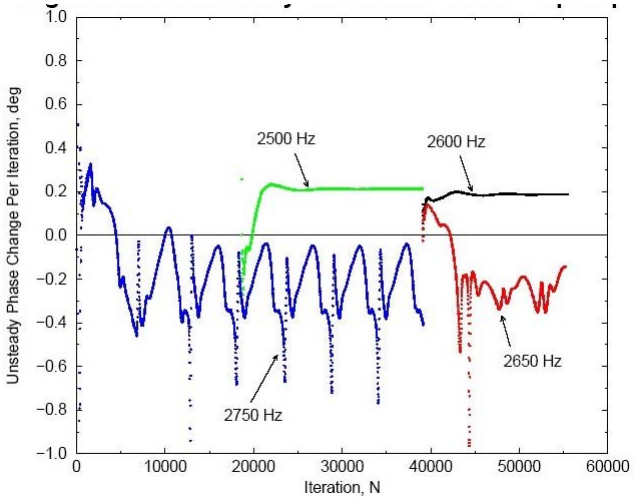

Figure 34. 3D C1 Case: Phase Change Per Iteration (IBPA = 0, 0.020 in. Running Tip Clearance, $p_{exit}/p_{exit,exp}$ = 1.000)

For this study, a 0.020 inch tip clearance was used in accordance with the experimental data and computational data obtained from TURBO. Due to the limitations of the HB method as discussed above, only the time domain results are presented for the running clearance case. The two main design parameters that were varied were the back pressure and the tip clearance. For the 0.020 inch case, two frequencies are present. However, one of the frequencies happens to be very low. In Figures 35 and 36, an FFT of the time domain results for the blade torque is presented for back pressures of 1.015

and 1.020. Figure 36 demonstrates the results in the 0-100 Hz range, where a very low frequency component is present in the solution. Furthermore, the time domain results for the mass flow rates for back pressures of 1.010, 1.015, 1.020 are presented in Figure 37 and compared with the results obtained experimentally (CAFD) and using TURBO. It is noted that the flow is steady for $p_{exit}/p_{exitCAFD} = 1.010$. Finally, Figure 38 shows the time history results for various back pressures for the running tip clearance case.

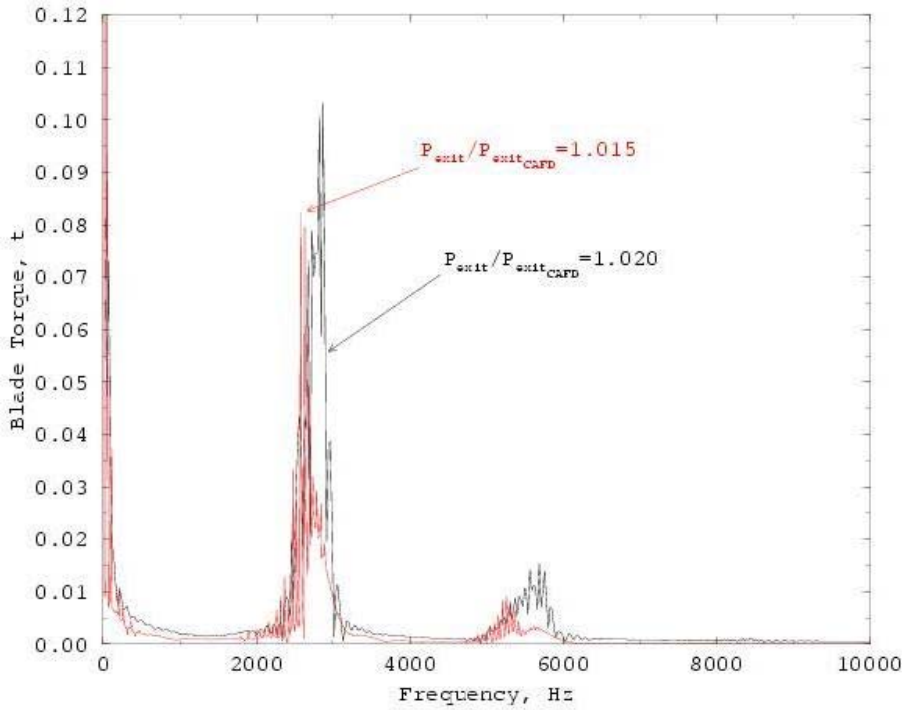

Figure 35. FFT of Blade Torque for Two Different Back Pressures (0.020 in. Running Tip Clearance)

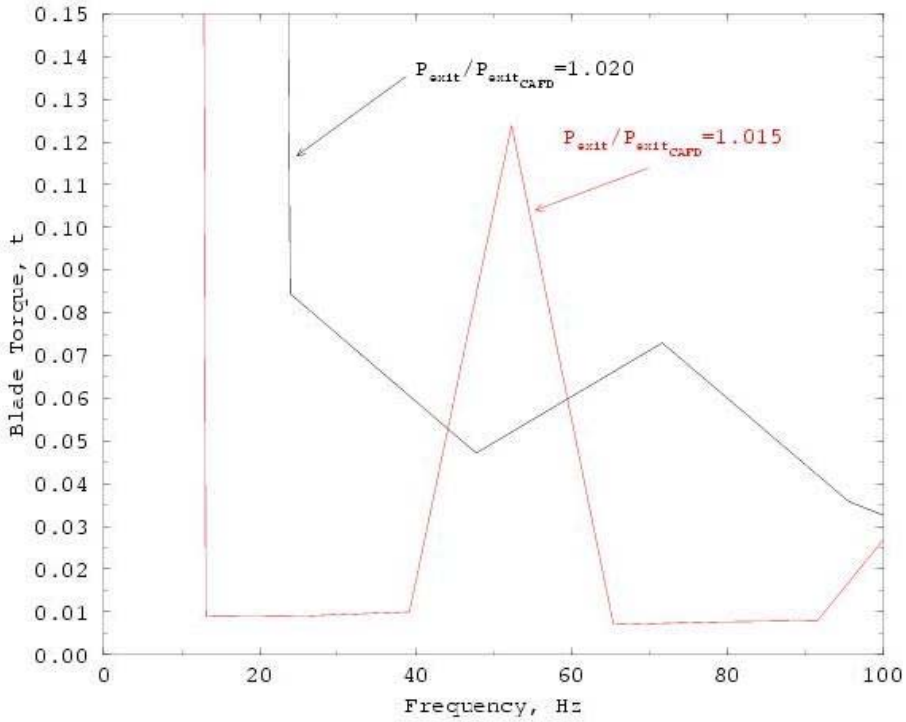

Figure 36. FFT of Blade Torque for Two Different Back Pressures (0.020 in. Running Tip Clearance) in Low Frequency Region

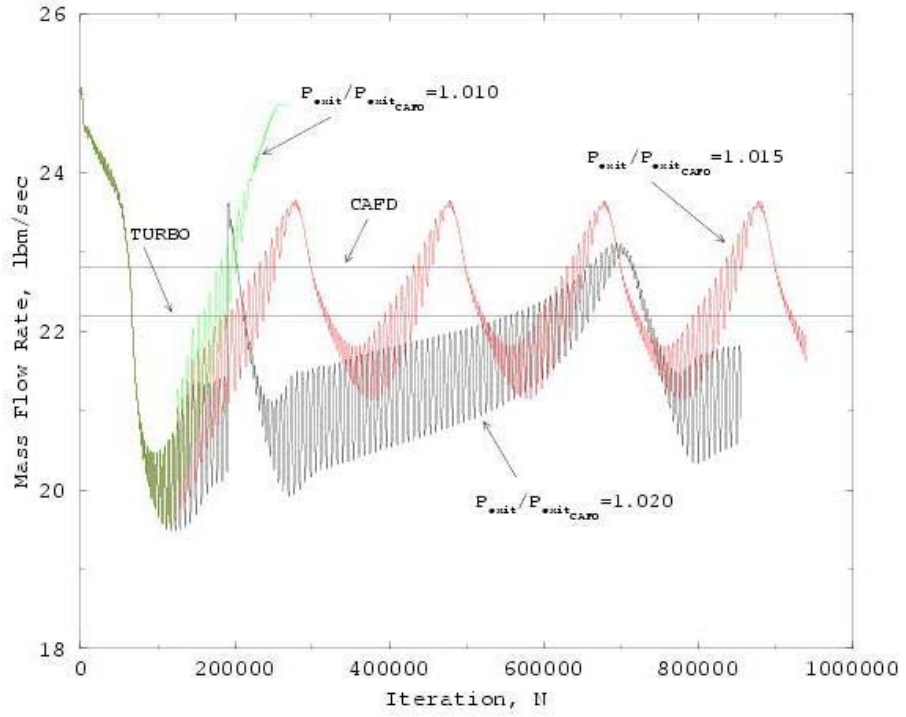

Figure 37. Time Domain Solution Mass Flow Rates for Different Back Pressures (0.020 in. Running Tip Clearance)

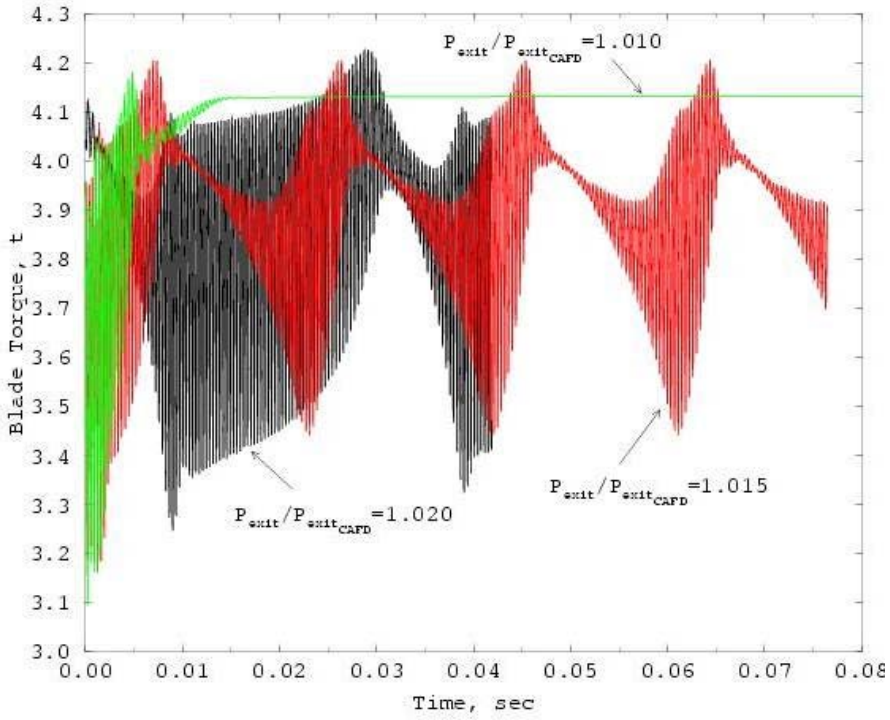

Figure 38. Time History of Blade Torque for Various Back Pressures (0.020 in. Running Tip Clearance)

Due to the limitations of the HB method to only handle one irrational frequency, a tight tip clearance case was also examined. Figure 39 shows time histories of blade torque for the tight tip clearance for two different back pressures and Figure 40 shows the FFT's of the time-domain solutions along with a HB result. As can be seen, HB shows good agreement for the lower back pressure case since there appears to be only a single frequency, and higher harmonics thereof, present in the time domain solution. However, the higher back pressure case has two distinct, irrational frequencies (beats) present, and HB can only handle one fundamental frequency and its harmonics. A summary of the NSV frequency results obtained can be found in Table 2. Some possible solutions to overcome the HB method's inability to handle more than one fundamental frequency are to extend the HB method to handle multiple irrational frequencies, use enforced motion to cause "lock-in" to the blade frequency, or use the aeroelastic solution to cause "lock-

in" to the non-linear flutter frequency (very near the blade frequency). All of these options are the subject of current research study.

		Clearance			
		Running (0.020 in.)		Tight (0.002 in.)	
		Time Domain	HB	Time Domain	HB
PR	PR = 1.000	No NSV	No NSV	f = 2000 Hz	f = 2000 Hz
	PR = 1.015	f_1 = 2650 Hz, f_2 = 50 Hz	X	f_1= 3200 Hz, f_2 = 3750 Hz	f_1 = 3200 Hz, f_2 = 3750 Hz
	PR = 1.020	f_1 = 2850 Hz, Low freq.	X	----------	----------

Table 2. Summary of Time Domain and HB Results for Both the Running and Tight Tip Clearances for Three Different Pressure Ratios

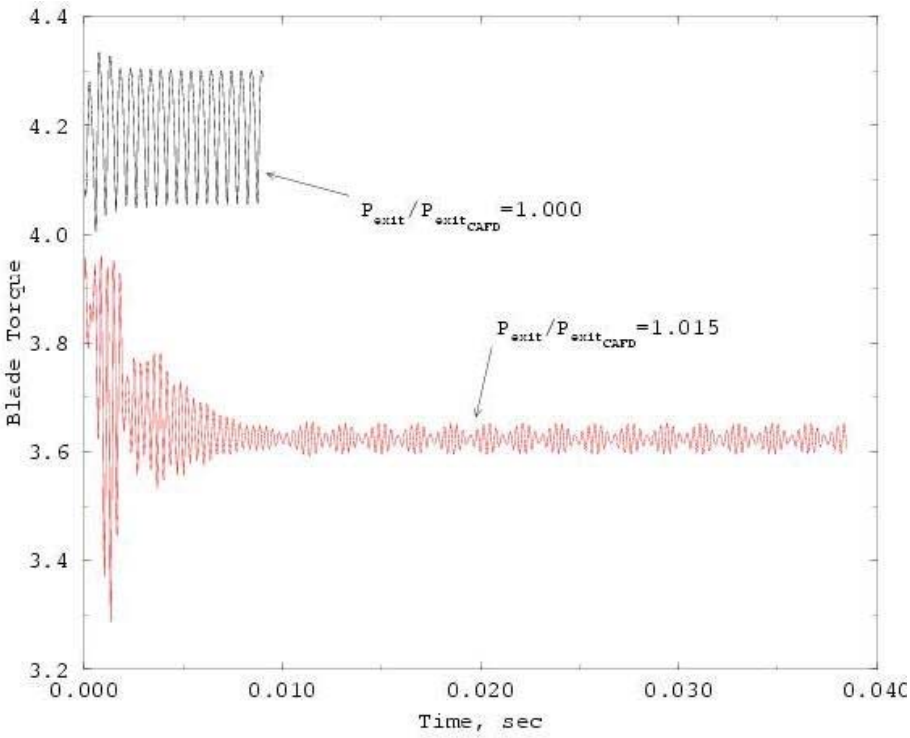

Figure 39. Time History of the Blade Torque for Two Different Back Pressures (0.002 in. Tight Tip Clearance)

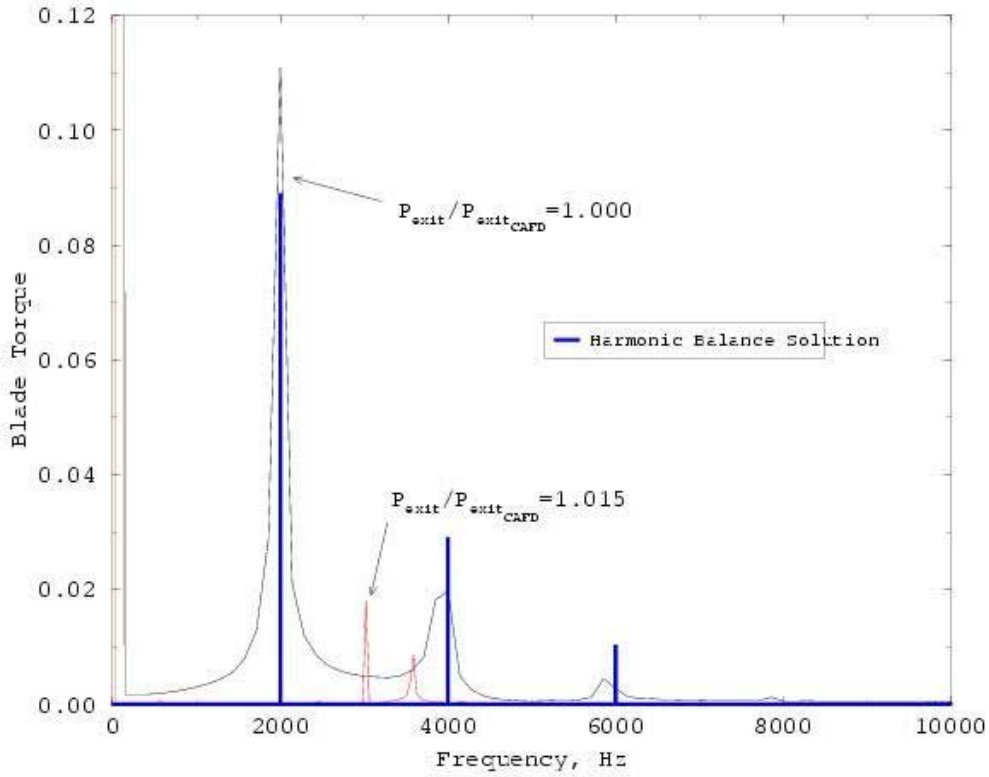

Figure 40. FFT of Blade Torque Compared with Harmonic Balance Solution (0.002 in. Tight Tip Clearance)

H1 CASE

Next, a study was conducted for a first stage modern fan blade (known as H1) that encountered flutter and not NSV. The GUIde Consortium members asked that an analysis be conducted to show that NSV is not predicted. As a result, both Euler and NS steady and unsteady analyses were performed. The steady analysis showed no signs of NSV. A linear flutter analysis was then conducted with the results compared to time domain results (TURBO) and is shown in Figure 41. There is reasonable agreement between the time and frequency domain results. The latest efforts involved reducing the back pressure to produce negative aerodynamic damping.

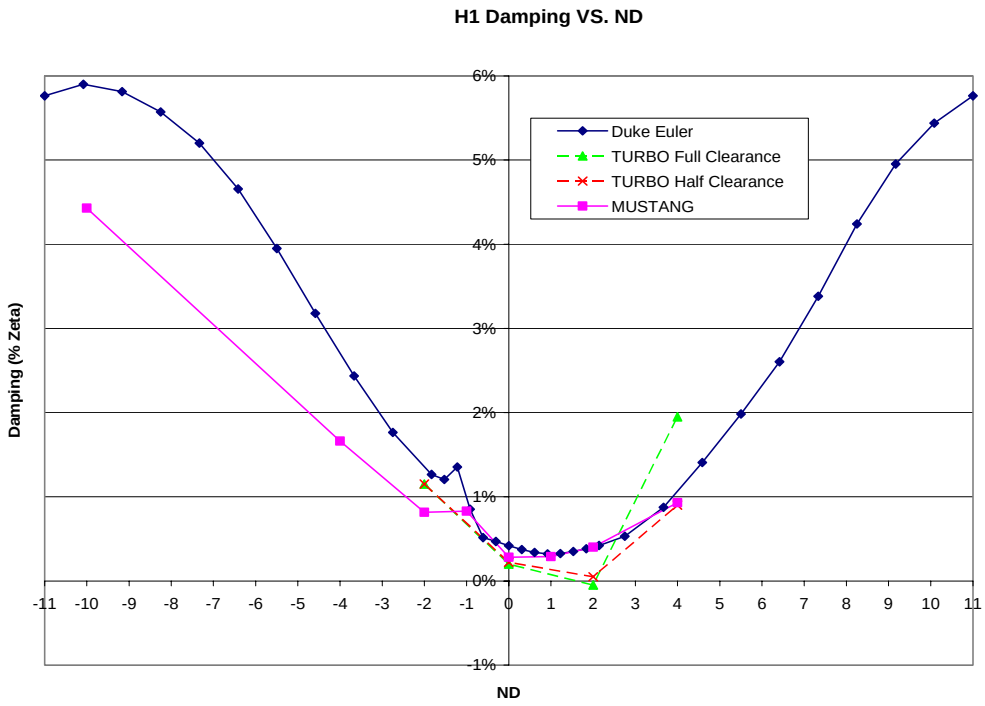

Figure 41. Time Domain and HB Results for Damping as a Function of Nodal Diameter for the H1 Case

H2 CASE

The final case that was studied was a modern fan vane blade known as the H2 case. This blade encountered NSV in experimental rig testing. An analysis was performed with TURBO and it showed good agreement with the experimental data. Since there is no clearance on a vane blade, this was thought to be a good test case for the HB method. However, the same problems were encountered as in the C1 case. Multiple irrational frequencies were present and the current HB method can only handle one fundamental frequency and its harmonics. Therefore, this case is still under investigation.

4. SUMMARY AND CONCLUSIONS

In recent years, new aeromechanical problems have been encountered in turbomachinery. In particular, non-synchronous vibrations in turbine blades have been

observed by many engine companies and occur as a result of a fluid dynamic instability such as shedding. If the oscillations become large enough, blade fatigue and failure can occur. It is difficult to predict because there is little knowledge of the phenomenon. As a result, there is a strong motivation to develop a fast computational method to be able to understand this behavior in the design stage.

For this study, many test cases were examined. As an initial demonstration of the method, the flow over a cylinder was investigated. This serves as a useful test case for modeling NSV because it is a well-studied phenomenon and a significant amount of experimental data is available. Next, this technique was extended to study the flow over a two-dimensional airfoil. In particular, we studied the 2D C1 case. Finally, the harmonic balance method was extended to three-dimensional cases from industry and compared with existing time domain solutions and experimental data. In particular, it was applied to the C1 case (a front compressor blade), the H1 case (a fan blade), and the H2 case (a fan vane). Therefore, there are numerous test cases available to test the harmonic balance method and establish it as a valuable design tool for future use by engine manufacturers.

The numerical approach involved the use of a two-dimensional nonlinear Navier-Stokes unsteady harmonic balance method developed by Hall, et al. One of the major advantages of this method is that it requires one to two orders of magnitude less computational time than conventional time marching CFD techniques. In addition, a unique phase error method was developed to determine the precise NSV frequency in only a few harmonic solution computations.

Next, the HB method was applied to the 2D C1 case from industry as well as the 3D C1, H1, and H2 cases. Preliminary results showed good agreement for the 2D case and promising results from the 3D cases. For the 3D C1 case, two main design parameters were varied – the tip clearance and the back pressure. Using the running tip clearance of 0.020 in., two irrational frequencies are present in the solution so the current HB method could not be used. However, time domain simulations were performed to determine the NSV frequency for three different back pressures. In an attempt to justify the merits of the HB method, a tighter tip clearance of 0.002 in. was studied. The HB method showed good agreement with the time domain results for the case of PR = 1.000 because only a single frequency and its harmonics were present for this case. Therefore, current research is focused on the following three methods to solve for the NSV frequency. One solution is to extend the HB method to handle multiple irrational frequencies. Other solutions are to use enforced motion to cause "lock-in" to the blade frequency or the aeroelastic solution to cause "lock-in" to the non-linear flutter frequency (very near the blade frequency) as was done in the study of the cylinder.

In addition, the H1 and H2 cases were studied. For the H1 case, the steady analysis showed no signs of NSV. A linear flutter analysis was then conducted and the results were compared to time domain results (TURBO). Reasonable agreement was achieved between the time and frequency domain results. The latest research efforts have involved reducing the back pressure to produce negative aerodynamic damping. Similar to the C1 case, the H2 case encountered multiple irrational frequencies present in the solution. Since the current HB method can only handle one fundamental frequency and

its harmonics, the methods described above are being implemented. This case is still under investigation.

Therefore, the harmonic balance method has been established as a viable tool to solve highly nonlinear unsteady shedding flow over turbine blades, the ultimate goal of the research effort. The results are consistent with those obtained by TURBO, a high fidelity computational tool. In addition, the HB method is able to predict both the NSV frequency and amplitude for the cylinder case and the 2-D C1 airfoil case but only for some 3-D flows. This is due to the presence of multiple NSV frequencies, which the current HB method cannot handle. Research is underway to address this problem and possible solution techniques are presented above. This method is a valuable design tool because the frequency can be added to the Campbell diagram to identify regions where the vortex shedding frequency may interact with the blade natural frequencies. Furthermore, it will allow engineers to better understand NSV behavior and to predict its occurrence in the design stage for flow over turbine engine blades.

REFERENCES

Anagnostopoulos, P., ed. *Flow-Induced Vibrations in Engineering Practice*. Boston: WIT Press, 2002.

Anagnostopoulos, P. and P.W. Bearman. "Response Characteristics of a Vortex-Excited Cylinder at Low Reynolds Numbers." *Journal of Fluids and Structures* 6 (1992): 39-50.

Anderson, Dale A., John C. Tannehill, and Richard H. Pletcher. *Computational Fluid Mechanics and Heat Transfer*. New York: McGraw-Hill, 1984.

Blevins, Robert D. *Flow-Induced Vibration*, 2nd ed. New York: Van Nostrand Reinhold, 1990.

Camp, T.R. "A Study of Acoustic Resonance in a Low-Speed Multistage Compressor." *ASME Transactions Journal of Turbomachinery* 121 (1999).

Chen, J.P. and Briley, W.R. "A Parallel Flow Solver for Unsteady Multiple Blade Row Turbomachinery Simulations." ASME-2001-GT-0348 (2001).

Clark, W.S. and K.C. Hall. "A Time-Linearized Navier-Stokes Analysis of Stall Flutter." *Journal of Turbomachinery* 122 (2000): 467-476.

Davis, Roger L., Ron-Ho Ni, and James E. Carter. "Cascade Viscous Flow Analysis Using the Navier-Stokes Equations." *Journal of Propulsion* 3 (1987): 406-414.

Fox, Robert W. and Alan T. McDonald. *Introduction to Fluid Mechanics*. New York: John Wiley & Sons, Inc., 1992.

Hall, Kenneth C. "Modern Analysis For Complex and Nonlinear Unsteady Flows in Turbomachinery." In *A Modern Course in Aeroelasticity*, 4th ed., ed. Earl H. Dowell, 675-703. Norwell: Kluwer Academic Publishers, 2004.

Hall, Kenneth C. and E.F. Crawley. "Calculation of Unsteady Flows in Turbomachinery Using the Linearized Euler Equations." *AIAA Journal* 27 (1989): 777-787.

Hall, Kenneth C., Jeffrey P. Thomas, and W.S. Clark. "Computation of Unsteady Nonlinear Flows in Cascades Using a Harmonic Balance Technique." *AIAA Journal* 40 (2002): 879-886.

Hall, Kenneth C. et al. *Non-Synchronous Vibrations of Turbomachinery Airfoils*. Paper presented at 9th Turbine Engine High Cycle Fatigue Conference in Pinehurts, North Carolina, March 16-19, 2004, 1-10.

He, L. "Unsteady Flow and Aeroelasticity." In *Handbook of Turbomachinery*, 2nd ed., ed. Earl Logan, Jr. and Ramendra Roy, 257-307. New York: Marcel Dekker, Inc., 2003.

Henderson, Ronald D. "Details of the Drag Curve Near the Onset of Vortex Shedding." *Physics of Fluids* 7 (1995): 2102-2104.

Inoue, M. Kuroumaru, M., Tanino, T., and Furukawa, M. "Propagation of Multiple Short Length-Scale Stall Cells in an Axial Compressor Rotor." ASME Paper 99-GT-97 (1999).

Keefe, Roger T. "Investigation of Fluctuating Forces on a Cylinder in a Subsonic Stream, and of the Associated Sound Field." *The Journal of the Acoustical Society of America* 34 (1962): 1711-1714.

Kielb, R., Barter, J., Thomas, J.P. and Hall, K.C. "Blade Excitation by Aerodynamic Instabilities – A Compressor Blade Study." ASME Paper GT-2003-38634 (2003).

Kielb, Robert E., Kenneth C. Hall, and Jeffrey P. Thomas. *Non-Synchronous Vibration of Turbomachinery Airfoils*. Paper presented at the annual meeting of the Air Force Office of Scientific Research (AFOSR), Report F49620-03-1-0204, 2003.

Kielb, Robert E., et al. *Non-Synchronous Vibration of Turbomachinery Airfoils*. Paper presented at the annual meeting of the Air Force Office of Scientific Research (AFOSR), Report F49620-03-1-0204, 2004.

Koopman, G. "The Vortex Wakes of Vibrating Cylinders at Low Reynolds Numbers." *Journal of Fluid Mechanics* 28 (1967): 501-512.

Lenglin, G. and Tan, C.S. "Characterization of Wake- and Tip-Vortex Induced Unsteady Blade Response in Multistage Compressor Environment". 7th National Turbine Engine HCF Conference (2002).

Mailach, R. "Experimental Investigation of Rotating Instabilities in a Low Speed Research Compressor." Third European Conference on Turbomachinery – Fluid Dynamics and Thermodynamics (1999).

Mailach, R., Lehmann, I., and Vogeler, K. "Rotating Instabilities in an Axial Compressor Originating from the Fluctuating Blade Tip Vortex." ASME Paper 2001-GT-0299 (2000).

Mailach, R., Sauer, H., and Vogeler, K. "The Periodical Interaction of the Tip Clearance Flow in the Blade Rows of Axial Compressors." ASME Paper 2001-GT-0299 (2001).

Maple, Raymond C. "Adaptive Harmonic Balance Method for Unsteady, Nonlinear, One-dimensional Periodic Flows." Ph.D. diss., Air Force Institute of Technology, 2002.

Marz, J., Gui, X., and Neise, W. "On the Structure of Rotating Instabilities in Axial Flow Machines." ISABE 99-7252, Proceedings of the 14th International Symposium on Airbreathing Engines (1999).

Marz, J., Hah, C., and Neise, W. "An Experimental and Numerical Investigation into the Mechanisms of Rotating Instability." ASME Paper 2001-GT-0536 (2001).

McMullen, Matthew, Antony Jameson, and Juan J. Alonso. *Acceleration of Convergence to a Periodic Steady State in Turbomachinery Flows*. Paper presented at the 39th AIAA Aerospace Sciences Meeting & Exhibit in Reno, Nevada, January 8-11, 2001, 1-11.

McMullen, Matthew, Antony Jameson, and Juan J. Alonso. *Application of a Non-Linear*

Frequency Domain Solver to the Euler and Navier-Stokes Equations. Paper presented at the 40th AIAA Aerospace Sciences Meeting & Exhibit in Reno, Nevada, January 14-17, *2002*, 1-16.

Ni, Ron-Ho. "A Multiple-Grid Scheme for Solving the Euler Equations." *AIAA Journal* 20 (1982): 1565-1571.

Norberg, C. "Fluctuating Lift on a Circular Cylinder: Review and New Measurements." *Journal of Fluids and Structures* 17 (2003): 57-96.

Norberg, C. "Flow Around a Circular Cylinder: Aspects of Fluctuating Lift." *Journal of Fluids and Structures* 15 (2001): 459-469.

Sarpkaya, T. "A Critical Review of the Intrinsic Nature of Vortex-Induced Vibrations." *Journal of Fluids and Structures* 19 (2004): 389-447.

Tanida, Y., A. Okajima, and Y. Watanabe. "Stability of a Circular Cylinder Oscillating in Uniform Flow or in a Wake." *Journal of Fluid Mechanics* 61 (1973): 769-784.

Thomas, Jeffrey P., E. H. Dowell, and K.C. Hall. "Nonlinear Inviscid Aerodynamic Effects on Transonic Divergence, Flutter, and Limit Cycle Oscillations." *AIAA Journal* 40 (2002): 638-646.

Thompson, Mark C. and Patrice LeGal. *A Re-examination of the Stuart-Landau Model Applied to Cylinder Wake Transition*. Paper presented as part of the symposium "Conference on Bluff Body Wakes and Vortex-Induced Vibrations (BBVIV3)", Port Douglas, Australia, 1-4. Available from http://mec-mail.eng.monash.edu.au/~mct/pubs/pdfs/bbviv3b.pdf. Accessed 5 January 2004.

Vo, H.D. "Role of Tip Clearance Flow on Axial Compressor Stability." Massachusetts Institute of Technology (2001).

Williamson, C.H.K. "Vortex Dynamics in the Cylinder Wake." *Annual Review of Fluid Mechanics* 28 (1996): 447-526.

Williamson, C.H.K. and G.L.Brown. "A Series in $1/\sqrt{\mathrm{Re}}$ to Represent the Strouhal-Reynolds Number Relationship of the Cylinder Wake." *Journal of Fluids and Structures* 12 (1998): 1073-1085.

Williamson, C.H.K. and R. Govardhan. "Vortex-Induced Vibrations." *Annual Review of Fluid Mechanics* 36 (2004): 413-355.

Williamson, C.H.K. "Defining a Universal and Continuous Strouhal-Reynolds Number Relationship for the Laminar Vortex Shedding of a Circular Cylinder," *Physics of Fluids* 31 (1988): 2742-2744.